Univerzita Palackého v Olomouci
Přírodovědecká fakulta

Školící pracoviště:
Společná laboratoř optiky

DIPLOMOVÁ PRÁCE

Strojové učení pro optimalizaci kvantových hradel

Vypracoval:	**Jan Jašek**
Studijní obor:	1702T001 Aplikovaná Fyzika
Forma studia:	Prezenční
Garantující pracoviště:	Katedra experimentální fyziky
Vedoucí diplomové práce:	Doc. Mgr. Karel Lemr, Ph.D.
Rok:	2020

Palacky University in Olomouc
Faculty of Science

Supervising department:
Joint Laboratory of Optics

DIPLOMA THESIS

Machine learning for quantum gate optimization

Author:	**Jan Jašek**
Study program:	N1701 Fyzika
Field of study:	Applied physics
Form of study:	Full-time
Guaranteed by:	Department of Experimental physics
Supervisor:	Doc. Mgr. Karel Lemr, Ph.D.
Year:	2020

Declaration of originality

I hereby declare that I have prepared the submitted diploma thesis independently under the guidance of supervising professor doc. Mgr. Karel Lemr, Ph.D. and that I have used only the resources I quote and list in the Bibliography section.

In Olomouci, May 10, 2020

....
Jan Jašek

Bibliografická identifikace

Jméno a příjmení autora	Jan Jašek
Název práce	Strojové učení pro optimalizaci kvantových hradel
Typ práce	Diplomová
Garantující pracoviště	Katedra experimentální fyziky
Školící pracoviště	Společná laboratoř optiky Univerzity Palackého a Fyzikálního ústavu Akademie věd České republiky
Vedoucí práce	Doc. Mgr. Karel Lemr, Ph.D.
Rok obhajoby práce	2020
Abstrakt	Kvantové strojové učení je mladá disciplína kvantového zpracování informace, která využívá podobností principů kvantové mechaniky a metod strojového učení pro zpracování netypických dat či vzorů. V této práci ukážeme, jak experimentálně implementovat strojově učené kvantové hradlo ovládáné klasickým optimalizačním algoritmem. Učící schopnosti hradla demonstrujeme na problému fázově kovariantního klonování, které je hradlo schopno se naučit takřka optimálně, využívajíc zpětnou vazbu v podobě fidelit jednotlivých klonů. Práce je rozdělena do tří kapitol, první rozebírá základní principy kvantové mechaniky a kvantového zpracování informace, spolu se stručným úvodem do metod strojového učení a platformě lineární optiky. Druhá kapitola popisuje konstrukci a justáž vysokostabilního interferometru Mach-Zehnderova typu, který tvoří stěžejní část kvantového hradla. V poslední kapitole najdeme výsledky dvou experimentů, které ukazují, jak je možno algoritmizovat fázově kovarientní kloner metodami zpětnovazebného učení.
Klíčová slova	strojové učení, kvantové hradlo, kvantové klonování, interferometrie, lineární optika, foton
Počet stran	71
Počet příloh	1
Jazyk	Anglický

Bibliographical identification

Autor's first name and surname	Jan Jašek
Title	Machine learning for quantum gate optimization
Type of thesis	Master
Garanting department	Department of Experimental Physics
Supervising department	Joint Laboratory of Optics of Palacký University and Institute of Physics of Czech Academy of Science
Supervisor	Doc. Mgr. Karel Lemr, Ph.D.
The year of presentation	2020
Abstract	Quantum machine learning is a young field of quantum information processing that exploits the similarities in principles of both quantum mechanics and machine learning methods to process atypical data and patterns. In this thesis, we present an experimental realization of machine-learned quantum gate controlled by classical optimization algorithm. To demonstrate the gates capabilities to learn, we show that the gate can learn phase-covariant cloning to nearly optimal level, having the feedback in form of the fidelities of individual clones. The thesis is divided into three chapters, first of which explains basic principles of quantum mechanics and quantum information processing, together with a brief introduction to machine learning methods and the platform of linear optics. The second chapter describes the construction and alignment of highly stable Mach-Zehnder type interferometer, which represents a fundamental part of the presented quantum gate. In the third chapter, we present results of two experiments that show how to algorithmize and train a phase-covariant quantum cloner using reinforcement learning methods.
Keywords	machine learning, quantum gate, quantum cloning, interferometry, linear optics, photon
Number of pages	71
Number of appendices	1
Language	English

Contents

Introduction

Quantum theory offers the most advanced and precise way to describe natural phenomena that is currently available [2]. By introducing concepts such as superposition, entanglement, wave-particle dualism and tunneling, it presents the most detailed explanation of the behavior of elementary particles and waves. As a result, quantum physics allows us to explore a wide range of possible technological and research innovations, such as highly sensitive measurements in quantum metrology [3], and quantum information science [4].

Quantum information science is a modern scientific area that surpasses limitations of classical information theory. Its core concepts rely on quantum theory, and as such evolved hand in hand with new discoveries in quantum mechanics. Currently there are two major branches of quantum information science, quantum communications and quantum computing.

For instance, quantum cryptography exploits the principles of the quantum theory to create a secured communication channel, allowing to transfer information safely using quantum states [5]. In quantum mechanics, the process of measurement on a system causes the system to change its state, therefore by using certain communication protocols, the two communicating users can always detect any third party trying to eavesdrop on their communication. The security of the communication relies solely on quantum information theory and it cannot be broken even if the attacker has unlimited computer power available.

Quantum computing utilizes the qubit as a unit of quantum information, which theoretically contains infinite amount of classical information due to the principle of superposition, and quantum computer as such can theoretically solve problems which would be unsolvable by classical binary information systems [4]. Any observable change of information (e.g. changing bit from one to zero) is called information processing. Quantum information processing is a branch of quantum information science, which utilizes different physical platforms to manipulate qubits using quantum gates. Such platforms include quantum dots [6], trapped ions [7], superconducting circuits [8] and photons [9].

In recent years, classical information processing has witnessed a boom of machine learning techniques, that range from simple regressions to complex methods of optimization and pattern recognition [10]. At its heart, machine learning methods are based on matrix operations on high-dimensional vectors, hence interesting similarity with quantum mechanics [11]. As a result, a young field of quantum machine learning emerged and offered a promising way to process atypical patterns in data [12]. The overlap between quantum machine learning and quantum computing could create interesting alternative to classical information processing, both in the computational time needed for the task at hand and in the capability to process the data.

In this thesis, we present an experimental realization of machine-learned quan-

tum gate controlled by classical optimization algorithm. To demonstrate the gates capabilities to learn, we show that the gate can learn phase-covariant cloning to nearly optimal level, having the feedback in form of the fidelities of individual clones. The thesis is divided into three chapters, first of which explains basic principles of quantum mechanics and quantum information processing, together with a brief introduction to machine learning methods and platform of linear optics. Second chapter describes construction and alignment of highly stable Mach-Zehnder type interferometer, which represents a fundamental part of the presented quantum gate. In the third chapter, we present results of two experiments that show how to algorithmize and train a phase-covariant quantum cloner using reinforcement learning methods.

Chapter 1

Principles and methods

1.1 Quantum model of electromagnetic field and Fock states

First of all, let us briefly describe the electromagnetic field using the quantum theory. This process is usually referred to as quantization of electromagnetic field (also called the second quantization). We will only mention key aspects of the second quantization, as detailed description can be found in various literature, e.g. [13, 14] and goes beyond the scope of this thesis.

In classical physics, we describe electromagnetic field using Maxwell's equations in vacuum [15]

$$\boldsymbol{\nabla} \cdot \vec{B} = 0, \tag{1.1}$$

$$\boldsymbol{\nabla} \cdot \vec{D} = 0, \tag{1.2}$$

$$\boldsymbol{\nabla} \times \vec{E} = -\frac{\partial B}{\partial t}, \tag{1.3}$$

$$\boldsymbol{\nabla} \times \vec{H} = \frac{\partial D}{\partial t} + \vec{j}, \tag{1.4}$$

where vectors $\vec{E}$ and $\vec{H}$ denote electric and magnetic intensities, vector $\vec{D}$ denotes electric displacement field and $\vec{B}$ stands for magnetic induction with respective constitutive relations

$$\vec{D} = \varepsilon \vec{E}, \tag{1.5}$$

$$\vec{B} = \mu \vec{H}, \tag{1.6}$$

where ε stands for permittivity and μ for permeability. In vacuum, these quantities equal constant values $\varepsilon = \varepsilon_0$ and $\mu = \mu_0$, respectively.

Using these equations, we can define the energy density of the electromagnetic field in free space U as [15]

$$U = \frac{1}{2} \left(\varepsilon_0 |\vec{E}|^2 + \mu_0 |\vec{H}|^2 \right) \tag{1.7}$$

In theoretical mechanics, the total energy of a system is usually given by Hamiltonian H [16]. For a specific quadratic potential and using generalized coordinates, H takes the form of a sum of independent linear oscillators in the form of [14]

$$H = \sum_j \frac{1}{2} \left(|\vec{p}|_j^2 + \omega_j^2 |\vec{q}|_j^2 \right), \tag{1.8}$$

where $\vec{p}_j$ and $\vec{q}_j$ stand for generalized momentum and generalized position of jth oscillator, respectively and ω_j denotes angular frequency. We can see that the equation 1.8 formally resembles equation 1.7.

In the case of electromagnetic field, we can associate the corresponding jth oscillator with the jth mode (configuration) of electromagnetic field and the generalized coordinates with electric and magnetic intensities.

In quantum mechanics, the generalized coordinates and Hamiltonian are replaced by their operator forms and equation (1.8) can be rewritten as

$$\hat{H} = \sum_j \frac{1}{2} \left(|\hat{p}|_j^2 + \omega_j^2 |\hat{q}|_j^2 \right), \tag{1.9}$$

where $\hat{p}_j$ and $\hat{q}_j$ stand for the operators of momentum and position and $\hat{H}$ denotes the Hamiltonian operator (operator of total energy). These operators obey the commutation relations [2]

$$[\hat{q}_i, \hat{p}_j] = i\hbar \delta_{ij}, \tag{1.10}$$

$$[\hat{q}_i, \hat{q}_j] = [\hat{p}_i, \hat{p}_j] = 0, \tag{1.11}$$

where $\hbar$ is the reduced Planck constant, and equals $\hbar = \frac{h}{2\pi}$ (h is the original Planck constant).

Now given the formal correspondence of the classical electromagnetic field and classical linear oscillators, we can use the formalism of quantum linear oscillators to express quantized electromagnetic field. It is convenient to define the so-called creation operator $\hat{a}_j^\dagger$ and annihilation operator $\hat{a}_j$ (in quantum mechanics also referred to as ladder operators) for the jth mode as [13]

$$\hat{a}_j = \frac{1}{\sqrt{2m_j \hbar \omega_j}} \left(m_j \omega_j \hat{q}_j - i\hat{p}_j \right), \tag{1.12}$$

$$\hat{a}_j^\dagger = \frac{1}{\sqrt{2m_j \hbar \omega_j}} \left(m_j \omega_j \hat{q}_j + i\hat{p}_j \right), \tag{1.13}$$

where m_j is a constant with a dimension of mass. The commutation relations for these operators are similar to those between $\hat{p}_j$ and $\hat{q}_j$

$$\left[\hat{a}_i, \hat{a}_j^\dagger \right] = \delta_{ij}, \tag{1.14}$$

$$[\hat{a}_i, \hat{a}_j] = \left[\hat{a}_i^\dagger, \hat{a}_j^\dagger \right] = 0 \tag{1.15}$$

and can be used to express the Hamiltonian in a more elegant way

$$\hat{H}_j = \hbar \omega_j \left(\hat{a}_j^\dagger \hat{a}_j + \frac{1}{2} \right) = \hbar \omega_j \left(\hat{N}_j + \frac{1}{2} \right), \tag{1.16}$$

where $\hat{a}_j^\dagger \hat{a}_j = \hat{N}_j$ stands for the number operator in the jth mode.

Following Dirac's notation, let us now consider a system in energy eigenstate $|n_j\rangle$. It follows that

$$\hat{a}_j^\dagger \hat{a}_j |n_j\rangle = \hat{N}_j |n_j\rangle = n_j |n_j\rangle, \tag{1.17}$$

which shows that the energy eigenstate $|n_j\rangle$ is also the eigenstate of the number operator $\hat{N}_j$. The eigenvalues n_j actually correspond to the n_j quanta each having

energy $\hbar\omega_j$, which we call photons. The eigenstate $|n_j\rangle$ is called the Fock state and it represents the number of photons in a corresponding mode of the field.

Applying annihilation and creation operators on the Fock state gives us the following relations

$$\hat{a}\,|n\rangle = \sqrt{n}\,|n-1\rangle\,, \tag{1.18}$$

$$\hat{a}^\dagger\,|n\rangle = \sqrt{n+1}\,|n+1\rangle\,. \tag{1.19}$$

This means that applying annihilation operator on a state decreases the number of photons in the state by one. In contrast, applying creation operator on a state increases the number of photons by one.

If we consider vacuum state $|0\rangle$ (state with zero photons), applying annihilation and creation operators yields

$$\hat{a}\,|0\rangle = 0, \tag{1.20}$$

$$\hat{a}^\dagger\,|0\rangle = |1\rangle\,. \tag{1.21}$$

1.2 Qubit

It is a textbook knowledge that the elementary unit of classical information is a bit [17]. A bit can only take two discrete logical values, either 0 or 1, and any classical information is in fact expressed as a sequence of bits encoded into an object, such as a computer memory.

In quantum information processing, the quantum bit (qubit) takes place as the basic unit of information [4]. Unlike the classical bit which can only be in the state 0 or 1, the qubit capitalizes on the principle of superposition known from quantum theory. The principle of superposition states that if the object can be in several discerete valid states, it can also be in any linear combination of the states (so-called superpositions). This actually means that if we consider states $|0\rangle$ and $|1\rangle$ (notation $|\rangle$ corresponds to Dirac notation) our two logical states, i.e. so-called computational basis states, qubit can also be found in any linear combination of the basis states, e.g. $\frac{1}{\sqrt{2}}\left(|0\rangle + |1\rangle\right)$.

Formally, we can define qubit as normalized vector in two dimensional Hilbert space with ortonormal basis $|0\rangle\,,|1\rangle$. Qubit is a unit vector in this space that takes the form of

$$|\psi\rangle = \alpha\,|0\rangle + \beta\,|1\rangle\,, \tag{1.22}$$

where α, $\beta \in \mathbb{C}$ are probability amplitudes that satisfy normalisation condition $|\alpha|^2 + |\beta|^2 = 1$. We can interpret the modulus squared of the probability amplitudes as probabilities in a sense that when measuring qubit in the state $|\psi\rangle$, we have probability $|\alpha|^2$ of finding the qubit in the state $|0\rangle$ and probability $|\beta|^2$ of finding the qubit in the state $|1\rangle$. The superposition also means that there is no way to predict the outcome of this measurement, all we know about the qubit are the probabilities $|\alpha|^2$ and $|\beta|^2$.

Qubit can be physically realized by any two level quantum system (any quantum object that can be found in two discrete states). On the optical platform, qubit can be efficiently encoded using photons [18], either by encoding the qubit in photon polarization (polarization encoding) [19], or by its trajectory in some optical system (spatial encoding) [20], which is composed of multiple optical paths (e.g. optical fiber), in which the photon has non-zero probability to enter. If

there are two possible paths, we can also describe it as vector in two-dimensional Hilbert space. By increasing the number of paths, we can effectively increase the dimension of the Hilbert space (and also the number of basis vectors, thus having a general qudit [21]). There are other possible methods of encoding, namely time-bin [22] and orbital angular momenta [23], however the experimental setup presented in this thesis uses polarization encoding to prepare and detect qubits and spatial modes to selectively address transformations.

1.3 Photon polarization and polarization encoding

In homogeneous isotropic medium, electromagnetic radiation is a transverse wave made of two perpendicular vectors, electric field $\vec{E}$ and magnetic field $\vec{H}$ [24]. Vectors $\vec{E}$ and $\vec{H}$ are perpendicular both to each other and to the direction of the energy propagation which in homogeneous isotropic medium also corresponds to the direction of the wave propagation. Both the vectors change their magnitude and direction as the wave propagates, but always form a plane perpendicular to the direction of the propagation (a transverse wave). The polarization is then defined as the trajectory of one of the field vectors (in our case the vector $\vec{E}$) at discrete points in space in a plane perpendicular to the wave propagation.

If this trajectory is completely chaotic and doesn't follow any pattern, the light wave is unpolarized. If however the trajectory does follow a pattern in a periodic way, we call the light wave polarized. Generally, the trajectory corresponds to an ellipse, but in special cases, it becomes a circle (circular polarization) or a line (linear polarization). We can also denote $p \in [0,1]$ as degree of polarization, in which case $p = 1$ for polarized light and $p = 0$ for unpolarized light. Any other polarization state, corresponding to a number between zero and one, represents partially polarized light.

Mathematically, we can describe polarization of fully polarized light using Jones vector [25], which for light propagating in the direction of axis z can be written as

$$\vec{E} = \begin{pmatrix} E_x \\ E_y \end{pmatrix} = \begin{pmatrix} A_x \exp\left(i\delta_x\right) \\ A_y \exp\left(i\delta_y\right) \end{pmatrix}, \tag{1.23}$$

where A_x denotes real amplitude and δ_x phase of the x component of the field vector E_x (and equivalently for E_y). It is common to note phase difference of the x and y components as only the relative phase has a physical meaning, thus we can rewrite the equation as

$$\vec{E} = \begin{pmatrix} A_x \\ A_y \exp\left(i\Delta\right) \end{pmatrix}, \tag{1.24}$$

where $\Delta = (\delta_y - \delta_x)$ and we normalize the amplitudes with condition $|\vec{E}|^2 = 1$ to ensure that E is a unit vector. The combination of A_x, A_y, Δ gives us the resulting Jones vector, for example for $\Delta = 0$, we get linearly polarized light, horizontally $|H\rangle$ for $A_x = 1$, $A_y = 0$, vertically $|V\rangle$ for $A_x = 0$, $A_y = 1$ and diagonally $|D\rangle$ for $A_x = A_y = \frac{1}{\sqrt{2}}$. The corresponding Jones vectors are $\begin{pmatrix} 1 \\ 0 \end{pmatrix}, \begin{pmatrix} 0 \\ 1 \end{pmatrix}, \frac{1}{\sqrt{2}} \begin{pmatrix} 1 \\ 1 \end{pmatrix}$, respectively. For $\Delta \neq 0$, $A_x \neq 0$ and $A_y \neq 0$, we get non-linear polarizations, such as general elliptic or circular for $\Delta = \pm\frac{\pi}{2}$ and $A_x = A_y$.

Jones vector perfectly describes a polarization state of a single mode in so-called pure state. However, any mixture of waves with different polarizations (so called mixed state which actually corresponds to the partially polarized light) can not be described using this formalism and the correlations between the components of electric field can only by described stochastically, using statistics. In such cases, it is necessary to use more complex methods of description, such as coherency matrix or Stokes parameters [26]

$$S_0 = I \tag{1.25}$$

$$S_1 = Ip\cos(\alpha)\cos(\beta) \tag{1.26}$$

$$S_2 = Ip\sin(\alpha)\cos(\beta) \tag{1.27}$$

$$S_3 = Ip\sin(\beta), \tag{1.28}$$

where I stands for total intensity of the beam (usually normalized to unit magnitude), p is the degree of polarization, α phase and β elevation.

Probably the most illustrative way to visualize polarization state is by using the Poincaré sphere, which is actually a plot of three normalized Stokes parameters (neglecting the first one) in three-dimensional Cartesian coordinates [26]. This results in a sphere we can see in Figure 1.1. All pure polarization states lie on the surface of the sphere, while partially polarized states lie inside the sphere, with the center of the sphere representing completely unpolarized light. Furthermore, any two opposite points on the Poincaré sphere correspond to orthogonal polarization states (orthogonal Jones vectors).

Poincaré sphere is actually analogous to the Bloch sphere, which is the visualization of possible states of a qubit and it is therefore straightforward to map the qubit states onto the polarization states [4]. As we can see in Figure 1.1, if we choose orthogonal polarization states as a basis and use Dirac's notation of quantum state in such a way that state $|H\rangle$ represents horizontal polarization and state $|V\rangle$ represents vertical polarization, we can associate these states with basis vectors $|0\rangle$ and $|1\rangle$ of a qubit. Single photon can be prepared in any linear combination of the horizontal and vertical polarization, therefore single photon can be used to encode one qubit of information.

1.4 Photon pairs generation

We have introduced the concept of photons and polarization encoding, so now let us discuss the way of generating photons we can actually encode the information into. In our experimental setup, we used a process of spontaneous parametric down-conversion (SPDC) [27], which is a second order non-linear optical process. SPDC is a parametric process that occurs in non-linear optical materials, such as $LiIO_3$ (lithium iodate) or BBO (beta barium borate) which is actually used in the reported experiment [1]. The non-linear crystal serves as a catalyst for the parametric process in which the photons from a high intensity incident pump beam (usually laser beam) have a certain (although very small) probability of annihilating, creating two new time-correlated photons (usually called signal and idler). During the process, the quantum state of the material stays unchanged. This process has to fulfill the laws of energy and momentum conservation, which can be written as

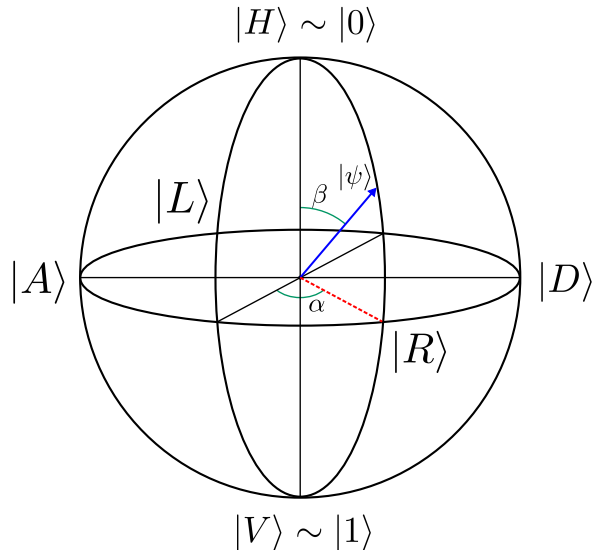$$\hbar\omega_p = \hbar\omega_s + \hbar\omega_i, \qquad \hbar\vec{k}_p = \hbar\vec{k}_s + \hbar\vec{k}_i, \tag{1.29}$$

Figure 1.1: Visualisation of polarization encoding using Poincaré sphere. While general qubit in state ψ is described by phase α and elevation β, the qubit state $|0\rangle$ corresponds to the polarization state $|H\rangle$ and qubit state $|1\rangle$ represents the polarization state $|V\rangle$. Other notable polarization states are represented − left-handed circular polarization $|L\rangle$, right-handed circular polarization $|R\rangle$, diagonal polarization $|D\rangle$ and anti-diagonal polarization $|A\rangle$. The center of the sphere represents unpolarized light, $p = 0$.

where $\vec{k}_i$ stands for wave vector and indexes p, s, i note pump, signal and idler beam, respectively.

Matching these conditions is sometimes referred to as phase matching and precise description of the process depends on the used non-linear material. Detailed description about non-linear crystals and non-linear processes in general can be found in various literature, such as [27, 28].

1.5 Linear optical platform

In this section, we will discuss how linear optical elements can be used to manipulate the photons and thus process the stored information. Namely we will describe two linear optical elements, which are used in our experimental setup, wave plates and polarization dependent beam splitter. The interaction itself can be always viewed as a linear transformation of complex amplitudes E of several spatial or polarization modes, hence we can describe it using linear algebra.

1.5.1 Beam splitter

The beam splitter is the major optical element used in any optical quantum gate, as it allows us to coherently superimpose (mix) spatial input modes. It can be physically realized as a fiber coupler, bulk cube or semitransparent plate and it is an essential part of every interferometer [14].

Let us now consider a classical mathematical description of a beam splitter that transforms two input modes into two output modes [14]. If we denote $E_{\mathrm{in},1}$ and $E_{\mathrm{in},2}$ the complex amplitude of incident light beams, $E_{\mathrm{out},1}$ and $E_{\mathrm{out},2}$ the amplitudes of the output (mixture of partially reflected and transmitted) light beams and r and t as the amplitude reflectance and amplitude transmittance

complex coefficients, the transformation matrix of the beam splitter takes form of

$$\begin{pmatrix} E_{\text{out},1} \\ E_{\text{out},2} \end{pmatrix} = \begin{pmatrix} t & r \\ -r & t \end{pmatrix} \begin{pmatrix} E_{\text{in},1} \\ E_{\text{in},2} \end{pmatrix}. \tag{1.30}$$

If we consider an ideal case in which beam splitter has zero absorbency, we also get a condition

$$|t|^2 + |r|^2 = 1, \tag{1.31}$$

which means that any input light on the beam splitter has to be partially transmitted or reflected (not absorbed) and for a special case of a single photon on the beam splitter, it is either transmitted or reflected. In a similar fashion, we can describe the ideal beam splitter using quantum mechanics, in which the complex amplitudes are replaced by annihilation and creation operators. The equation (1.30) then takes form of a unitary transformation

$$\begin{pmatrix} \hat{a}_{\text{out},1} \\ \hat{a}_{\text{out},2} \end{pmatrix} = \begin{pmatrix} t & r \\ -r & t \end{pmatrix} \begin{pmatrix} \hat{a}_{\text{in},1} \\ \hat{a}_{\text{in},2} \end{pmatrix}, \tag{1.32}$$

where $\hat{a}_{\text{in},1}$, $\hat{a}_{\text{in},2}$ are operators of the input spatial modes and $\hat{a}_{\text{out},1}$, $\hat{a}_{\text{out},2}$ are operators of the output spatial modes. We can also parametrize the beam splitter with single parameter η using relations [9]

$$t = \cos \eta, \qquad r = \sin \eta \tag{1.33}$$

and the equation (1.32) can be rewritten as

$$\begin{pmatrix} \hat{a}_{\text{out},1} \\ \hat{a}_{\text{out},2} \end{pmatrix} = \begin{pmatrix} \cos(\eta) & \sin(\eta) \\ -\sin(\eta) & \cos(\eta) \end{pmatrix} \begin{pmatrix} \hat{a}_{\text{in},1} \\ \hat{a}_{\text{in},2} \end{pmatrix}. \tag{1.34}$$

In our case, we also have to consider polarization states of photons as an additional mode that has to be taken in mind. For the purpose of splitting incident photon beams based on the photons polarization, we need optical elements sensitive to the polarization, such as a polarizing cube. This can be viewed as a special case of polarization dependent beam splitter [29]. If we yet again choose horizontal and vertical polarization states as our polarization basis, we can mathematically describe such a beam spliter by generalising equation (1.34) by increasing the number of both input and output modes to four, consisting of two horizontally polarized and two vertically polarized spatial modes

$$\begin{pmatrix} \hat{a}_{\text{Hout},1} \\ \hat{a}_{\text{Vout},1} \\ \hat{a}_{\text{Hout},2} \\ \hat{a}_{\text{Vout},2} \end{pmatrix} = \begin{pmatrix} \cos(\eta_{\text{H}}) & 0 & \sin(\eta_{\text{H}}) & 0 \\ 0 & \cos(\eta_{\text{V}}) & 0 & \sin(\eta_{\text{V}}) \\ -\sin(\eta_{\text{H}}) & 0 & \cos(\eta_{\text{H}}) & 0 \\ 0 & -\sin(\eta_{\text{V}}) & 0 & \cos(\eta_{\text{V}}) \end{pmatrix} \begin{pmatrix} \hat{a}_{\text{Hin},1} \\ \hat{a}_{\text{Vin},1} \\ \hat{a}_{\text{Hin},2} \\ \hat{a}_{\text{Vin},2} \end{pmatrix}, \tag{1.35}$$

where indexes H and V stand for horizontal and vertical polarization and η_{H}, η_{V} for generally unequal splitting rations for individual polarizations. Note that in this particular basis, the orthogonal polarization modes do not mix.

1.5.2 Wave plate

Wave plates are birefringent optical elements that allow us to control polarization state of a light beam by causing relative phase shift Γ between the H and V modes

of the wave. This is done by propagating along the wave plate fast and slow optical axis [30]. Formally, we can describe adding a phase shift as a transformation

$$\begin{pmatrix} \hat{a}_{\text{H,out}} \\ \hat{a}_{\text{V,out}} \end{pmatrix} = \begin{pmatrix} \cos(\nu) & -\sin(\nu) \\ \sin(\nu) & \cos(\nu) \end{pmatrix} \begin{pmatrix} \exp\left(i\frac{\Gamma}{2}\right) & 0 \\ 0 & \exp\left(-i\frac{\Gamma}{2}\right) \end{pmatrix}$$
$$\begin{pmatrix} \cos(\nu) & \sin(\nu) \\ -\sin(\nu) & \cos(\nu) \end{pmatrix} \begin{pmatrix} \hat{a}_{\text{H,in}} \\ \hat{a}_{\text{V,in}} \end{pmatrix} \tag{1.36}$$

where Γ represents the imposed phase shift and ν stands for the angle between wave plate fast axis and horizontally polarized component of the wave.

Wave plates are usually made of anisotropic material and common types are the half-wave plate, which causes a relative phase shift of $\Gamma = \pi$ between polarizations along wave plates fast and slow axis. This wave plate is often used to rotate linearly polarized light (horizontally to vertically and vice versa). The other notable type is a quarter-wave plate, which causes relative phase shift of $\Gamma = \frac{\pi}{2}$ and can be used to convert linearly polarized light into circularly polarized light (and vice versa) [31]. Combining two quarter-wave plates and one half-wave plate allows us to change any pure polarization state to any other polarization state.

The transformation caused by a half-wave plate can be described as [25]

$$\begin{pmatrix} \hat{a}_{\text{H,out}} \\ \hat{a}_{\text{V,out}} \end{pmatrix} = \begin{pmatrix} \cos(2\nu) & \sin(2\nu) \\ \sin(2\nu) & -\cos(2\nu) \end{pmatrix} \begin{pmatrix} \hat{a}_{\text{H,in}} \\ \hat{a}_{\text{V,in}} \end{pmatrix} \tag{1.37}$$

and the matrix transformation of quarter-wave plate then takes form of [9]

$$\begin{pmatrix} \hat{a}_{\text{H,out}} \\ \hat{a}_{\text{V,out}} \end{pmatrix} = \frac{1}{\sqrt{2}} \begin{pmatrix} 1 - i\cos(2\nu) & -i\sin(2\nu) \\ -i\sin(2\nu) & 1 + i\cos(2\nu) \end{pmatrix} \begin{pmatrix} \hat{a}_{\text{H,in}} \\ \hat{a}_{\text{V,in}} \end{pmatrix}. \tag{1.38}$$

1.6 Quantum cloning

In general, cloning can be described as an operation of selecting N identical input objects and creating M identical output objects. The most trivial process of cloning takes only one input object and creates two copies of it on the output (denoted as $1 \rightarrow 2$ cloning). In quantum cloning, we do not clone the object itself, but rather the quantum state $|\psi\rangle$ of the cloned object. That means that given qubit encoded in a particular quantum state, cloning the state yields us the same two copies of the qubit. This is an analogous process to the copying of a classical bit, however, it turns out that in quantum mechanics, perfect cloning is not possible [4].

1.6.1 No cloning theorem

In 1982, a letter entitled "A single quantum cannot be cloned" by Wooters and Zurek was published in Nature [32]. The paper contained a simple proof later known as the no cloning theorem which arrived at a simple conclusion: an arbitrary unknown quantum state cannot be perfectly cloned, which means that it is impossible to create its identical copy. How about an imperfect cloning though? If we consider the approximate copies of the cloned quantum state as valid clones as well, we can actually extend the cloning process to any quantum state. This was shown in 1996 by Bužek and Hillary [33].

The similarity of the cloned states, or rather the resemblance between the original and the copy can be described using fidelity $F \in [0; 1]$. Mathematically, fidelity between two states is defined as [4]

$$F\left(\hat{\rho}, \hat{\sigma}\right) = \left[\mathbf{Tr}\sqrt{\sqrt{\hat{\rho}}\,\hat{\sigma}\sqrt{\hat{\rho}}}\right]^{2}, \tag{1.39}$$

where $\hat{\sigma}$, $\hat{\rho}$ are density matrices of the two generally mixed states. In a special case in which $\hat{\sigma} = |\psi_\sigma\rangle\langle\psi_\sigma|$ represents pure quantum state, the equation simplifies to the form

$$F\left(|\psi_\sigma\rangle, \hat{\rho}\right) = \langle\psi_\sigma|\,\hat{\rho}\,|\psi_\sigma\rangle, \tag{1.40}$$

that can be interpreted as an overlap between $|\psi_\sigma\rangle$ and $\hat{\rho}$. For both $\hat{\sigma}$ and $\hat{\rho} = |\psi_\rho\rangle\langle\psi_\rho|$ being pure states, the equation yields

$$F\left(\hat{\sigma}, \hat{\rho}\right) = |\langle\psi_\sigma|\psi_\rho\rangle|^{2}. \tag{1.41}$$

In case of cloning, we label $|\psi_{\text{in}}\rangle$ the pure input quantum state and $\hat{\varrho}_{\text{i}}$ represents the reduced density matrix of the ith output state [34]. We can define fidelity of each of the M output clones as $F_{\text{i}} = \langle\psi_{\text{in}}|\,\hat{\varrho}_{\text{i}}\,|\psi_{\text{in}}\rangle$. Reduced density matrix $\hat{\varrho}_{\text{i}}$ can be obtained from the density matrix $\hat{\varrho}$ of the entire output state by applying partial trace over the other clones, $\hat{\varrho}_{\text{i}} = \mathbf{Tr}_{i\neq j}\,\hat{\varrho}$, $i \in [1, M]$, where M stands for the total number of output clones.

If the cloned output state is exactly the same as the original, the fidelity of ith clone equals $F_{\text{i}} = \langle\psi_{\text{in}}|\,\hat{\varrho}_{\text{i}}\,|\psi_{\text{in}}\rangle = 1$. If, however, the resulting output state is equal to a completely random stochastic mixture of states, we get average fidelity $\bar{F} = \frac{1}{D}$ for a general qudit and $\bar{F} = \frac{1}{2}$ in a case of a qubit.

1.6.2   Cloners

There are several properties we can use to characterize the devices used for cloning, namely: optimality, symmetry, success probability, ratio $N \rightarrow M$ (input to output clones), universality and principle of operation.

An optimal cloner is able to clone with maximum obtainable fidelity, for a given set of parameters: input-output cloning ratio, symmetry and a prior knowledge about the cloned states. The maximum possible fidelity differs for every particular class of cloned quantum states [34]. We can visualize this using Bloch sphere (see Fig. 1.1). For example, given the qubits that lie on the equator, the maximum clones' fidelity would differ from cloning fidelity of the states with different distribution on the sphere. If the resulting fidelity is below theoretical maximum, then the cloner is not optimal.

Symmetrical cloner achieves the cloning task in a way that all the fidelities of individual output clones are equal. Asymmetrical cloner can create the output clones each with different fidelity. We can also get a situation in which for example we create three clones, two with the same fidelity and one with different one, in which case we can denote the cloning process as $1 \rightarrow 2 + 1$.

The deterministic cloner performs the cloning transformation successfully in every realization of the cloning. For probabilistic devices, there is always a nonzero probability that the transformation fails and the quantum information is lost [34].

Universal cloner can clone any quantum state from the Bloch sphere with the same fidelity. Nonuniversal cloner specializes in cloning only certain class of quantum states, a subset of the Bloch sphere, for example only the states that lie on a plane parallel to the equator, but can achieve higher fidelity as the optimality varies for different classes of states.

Last property that defines a quantum cloner is its principle of operation. We can distinguish three basic types. Note that in these examples, the number of input states $N = 1$, even though for every output state we need and ancillary photon, which serves as a blank medium for the clone. From this point on, we will also limit the relations for a general qudit to qubit only.

The **Semi-classic cloner** measures the input quantum state against a random projection basis and stores the result of that measurement. If the result is for example $|H\rangle$, it then creates M copies with the same quantum state $|H\rangle$. If we choose the measurement basis randomly for every input state, we get maximum obtainable fidelity of $F = \frac{2}{3}$ which is referred to as semi-classical limit for quantum devices. However, the fidelity of the output clones is independent of its quantity.

Trivial cloner simply adds another random quantum state to the input quantum state and stochastically swaps them, so it is unclear which output is the original and which is the copy. The result is asymmetrical as for $M = 2$ output clones, one has fidelity $F = 1$ and the other $F = 0.5$, with the average fidelity $F = 0.75$. The output fidelity also depends on the number of the output photons and it decreases to the limit of $F = \frac{1}{2}$ as the number of output photons increases.

Quantum cloner uses some kind of quantum operation to improve the resulting fidelities of the cloned states. For a universal quantum cloner that can clone any quantum state, the maximum produced fidelity equals $F = \frac{5}{6} \approx 0.833$ for $M = 2$ and it decreases as M increases [33].

There are several realizations of quantum cloners each performing different quantum cloning process with different maximal theoretical fidelity. Comparing single types of cloners in detail is beyond the scope of this thesis and can be found in several papers, e.g. [34, 35]. In this thesis, we present a symmetrical phase covariant $1 \rightarrow 2$ cloner [36], which is the type used for an attack on the cryptographic protocols BB84 [5] and RO4 [37, 38].

We have noted that apart from semi-classic cloning, the resulting fidelities decrease as M increases. This is also dependent on the number of input photons N and the dimension of the the qudit (as mentioned in the section 1.2). For $N = 1$ and dimension 2 (qubit), we can plot the fidelity as a function of M as in Fig. 1.2 [39].

1.6.3 Phase covariant quantum cloning

Phase-covariant quantum cloning is defined as a transformation that is optimal for a restricted set of pure input states in the form of [36]

$$|\psi\rangle = \frac{1}{\sqrt{2}} \left(|0\rangle + \exp(i\alpha)|1\rangle\right), \qquad (1.42)$$

where α corresponds to the angle marked in Fig. 1.1 These states are referred to as equatorial states, as they are located at the equator of the Bloch sphere and are frequently used in the field of quantum cryptography [36].

The phase covariant quantum cloner can also clone states on planes parallel to the equator, which satisfy the condition that the fidelity of output clones is
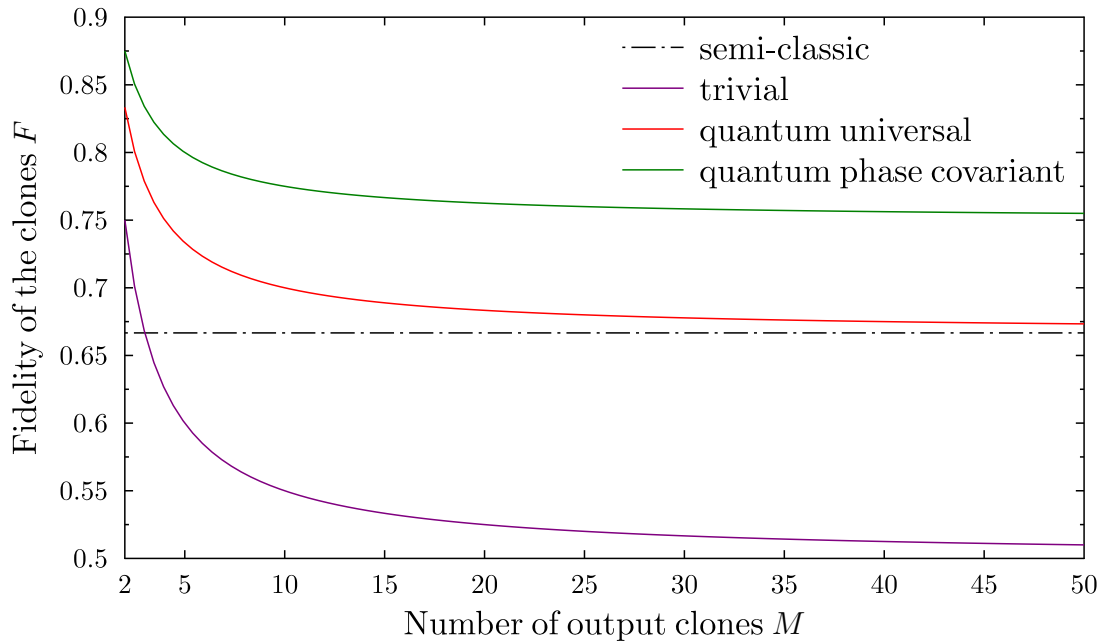
Figure 1.2: Fidelity of the output clones as a function of its number M for above mentioned cloning devices. The number of input states is $N = 1$ and the dimension of the qudit is 2.

invariant of the phase $\alpha \in [0, 2\pi]$ and only depends on the elevation $\beta \in [0, \pi]$ (see Fig. 1.1), that corresponds to the angle between the Bloch vector and the z axis of the Bloch sphere. The class of phase covariantly cloneable states are thus in general made of parallels on Bloch sphere and they can be mathematically described as

$$|\psi\rangle = \cos\left(\frac{\theta}{2}\right)|0\rangle + \exp(i\phi)\sin\left(\frac{\theta}{2}\right)|1\rangle. \tag{1.43}$$

The optimal transformation of the phase covariant states from the upper hemisphere reads [40]

$$|H\rangle |H\rangle \to |H\rangle |H\rangle, \qquad |V\rangle |H\rangle \to \frac{1}{\sqrt{2}}\left(|V\rangle |H\rangle + |H\rangle |V\rangle\right), \tag{1.44}$$

where the first state is the original cloned state and the second state is an ancillary state. For the lower hemisphere, the ancillary photon has to be vertically polarized and the transformation interchange state $|H\rangle$ for $|V\rangle$ and vice versa.

The theoretical maximum obtainable fidelity of the phase covariant quantum cloners differs with the respect to the angle β, with minimum fidelity $F = \frac{1}{2}\left(1 + \frac{1}{\sqrt{2}}\right) \approx 0.8535$ at the equator $(\beta = \frac{\pi}{2})$ and maximal at the poles of the Bloch sphere $(\beta = 0$ or $\beta = \pi)$.

1.7 Machine learning algorithms

For a last decade, machine learning has been experiencing increased popularity among both academic research and technology development. From simple logistic regressions to support vector machines, complex neural networks and deep learning, the power to find hidden patterns in data, identify and classify clusters or

22

learn from a feedback to improve performance over specific task has been extensively used in various fields, being it web security, medical science [41], automotive or targeted advertisement [42].

The classical engineering algorithmic problem solving approach usually consists of acquiring a necessary knowledge of the problem, building a mathematical model and implementing an algorithm based on this model [43]. In contrast, machine learning methods partially replaced the knowledge with sufficiently large number of known examples, known as training set, which is fed to a learning algorithm, essentially creating a Black box problem solving machine [44].

The learning algorithm itself is just a process of mapping the training set (data) to fit the machine parameters via minimizing a certain function (so called cost function C). The cost function can be just as simple as least squares method, which basically represents summing the squares of difference between the output of the machine and the actual expected output. Averaging the results over the whole training set yields us a single number describing how good or bad the parameters are. Optimization algorithms that minimize the cost function over all the machine parameters lie at the very heart of the machine learning. There are number of minimizing algorithms that are frequently used and they are usually sorted to gradient (e.g. gradient descent [45]) and nongradient (e.g. Nelder-Mead simplex algorithm [46]) methods.

Even though the recent boom in machine learning methods made summarizing this field rather difficult, machine learning methods are usually divided into three recognized categories: supervised learning, unsupervised learning and reinforcement learning [10].

The supervised learning is probably the most famous of the three, as it powers the best known examples of machine learning, being it image and speech recognition, spam classification, prediction or medical diagnoses. The basic idea of supervised learning is to create a large data set with the knowledge of some labels that describe the data, and then use this a priory knowledge in predicting the label of new incoming data. In human mind, the process itself is quite simple, for example considering the spam filter, all we have to do is go through of couple of hundreds of emails and then you will probably recognize whether a newly acquired email is a spam or not [42]. In a computer world, however, you do have to parametrize this task somehow, in order for the computer to store the relevant information. The task of identifying and mapping the set of parameters is usually nontrivial and requires a great deal of experimenting, which is why there are so many different techniques (e.g. neural networks with different sets of neurons and layers, each reaching a different performance for a specific task).

Unsupervised learning is somewhat of an opposite to the supervised learning. It is most commonly used to separate the data set into groups or clusters, which have something in common, to organize them in some way. This idea alone is intriguing in many fields as majority of the world data is actually unlabeled [10]. These data driven algorithms are best known in recommender systems at the web shops or pages like YouTube or Netflix, or in grouping the users on social networks with respect to their interests.

Conceptually very different, the basic idea of reinforced learning is to imitate the learning process of an ordinary human, which can be (from the very simple perspective) described as performing a task, failing horribly at it, doing it again, this time differently and possibly noticing a slight improvement in the task

performance [10]. By executing the task for quite some time, there will notable difference in which factors (parameters) improve the task performance and which do not, and anyone will do one's best to remember them, essentially learning from the past mistakes.

In a world of reinforcement learning, the computer is usually referred to as agent, which affects its environment with its possible actions, as it can be seen in Fig. 1.3. The environment responds back to the agent (often throughout an observing interpretor) with its updated state and a feedback, which can be thought of as a reward for the agents behavior. After a certain learning period, the agent is tested against a case that was not included in the training and if its performance improves, the learning is considered successful. The reinforced learning has been mostly used in training computer to play video games or simulations [47], as well as in this thesis.
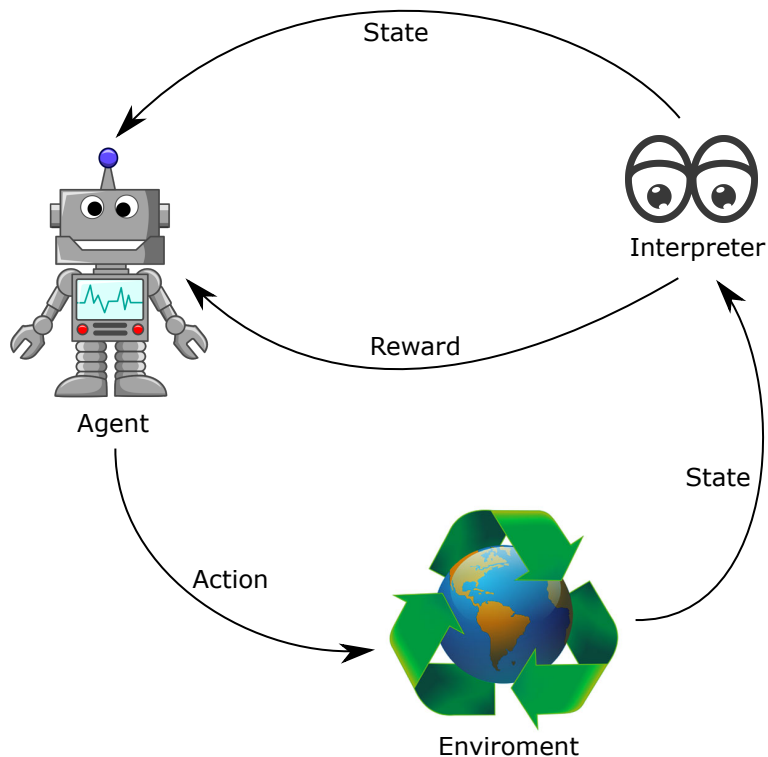

Figure 1.3: Reinforcement learning frame. The agent affects an enviroment with an action, the state of the enviroment is observed by the interpreter which evaluates the reward and passes it along with the enviroments state back to the agent. Adopted and adjusted from http://clipart-library.com/.

1.7.1 Quantum machine learning

More recently, the field of quantum machine learning (QML) rose as a possibly perspective overlap between quantum physics and machine learning algorithms [11]. It is well known that quantum computing reduces the computational difficulty of certain classes of problems (so called quantum speedup), for the same reason it is expected that the QML can help recognize atypical patterns of data that quantum mechanics often produce. Both machine learning methods and quantum mechanics also share the same mathematical toolkit as solving prob-

lems in both fields typically involves using matrix operations on high dimensional vectors.

The quantum speedup can be as high as exponential for certain problems, such as Shor's factoring algorithm or basic linear algebra subroutines, and is always conditioned by finding efficient quantum algorithm for solving problems [11] (if it exists) and limited by the experimental error of available technological devices. Another example of quantum algorithm outperforming best known classical algorithms can be search of an unsorted dataset with N entries. While the classical algorithms take time proportional to N, the quantum algorithm can search the dataset in time proportional to $\sqrt{N}$ and as such achieves a square root speedup.

We can distinguish four types of QML with respect to the input data and the processing algorithms, CC (classical data and classical data processing) which represents classical machine learning, QC (quantum input data and classical data processing), CQ (classical data and quantum data processing) and QQ (quantum input data and quantum data processing).

Variety of QML experiments were proposed, for example, in the paper [48], authors use small-scale photonic quantum computer to assign a cluster to high-dimensional vectors represented by quantum states, and then use the results as training set for implementing both supervised and unsupervised machine learning methods to classify future vectors.

In report [49], authors use formal similarity of quantum computing and machine learning kernel methods and interpret encoding of input data into quantum states as a feature map, which allows them to associate quantum Hilbert space with a high-dimension feature space. The quantum device can then use inner products of quantum state to compute kernel, which can be used by a variety of classical kernel methods, i.e. support vector machines.

Several papers regarding quantum reinforcement learning were also published. For example, in [50, 51], authors use machine learning methods, namely particle swarm optimization and differential-evolution, to eliminate guesswork in quantum measurement schemes employing adaptive feedback and apply it to the problem of interferometric phase estimation.

In a field of deep learning, papers regarding Boltzmann machines, one of the simplest types of neural networks, were proposed. In another report [52], the authors show that an artificial neural network can be trained to classify separability of quantum states with only partial information about the states available and achieves 98.3 % average match rate. Adding hidden layer to the neural network further improves the classification to average match rate of 99.7 %.

1.7.2   Nelder-Mead algorithm

As a powerful and robust way of finding a minimum of N-dimension fuctions without the need of a gradient, Nelder-Mead simplex algorithm was presented way back in 1965 [46] and is still commonly used in optimization algorithms, for example the *fminsearch* function in Matlab or *fmin* function in the Python Scipy module.

The Nelder-Mead simplex algorithm minimizes a chosen cost function C in a multidimensional space with the dimension corresponding to the number of the function parameters N. The algorithm takes $(N + 1)$ points in the parameter space to create a $(N + 1)$ dimensional initial simplex S (each point corresponds

to one of the simplex vertices). For example, with 2 parameters being optimized, the algorithm creates a triangle, for 3 parameters it creates a tetrahedron and so on.

The value of the cost function at each vertex of the simplex is then evaluated, the algorithm calculates the centroid c of the best side (side opposite of the vertex V_{H} with highest value of C) and then transforms the simplex in order to find a point of local minimum. The algorithm can transform the simplex in four ways, reflect, expand, contract and shrink (see Fig. 1.4, where the new simplex is displayed in blue color). The algorithm always tries to calculate as few vertices as possible, so it prioritizes on replacing the worst vertex via using reflection, expansion or contraction (the new test points always lie on the line along V_{H} and c). If any of these operations do not yield better result, the algorithm shrinks the simplex towards the vertex V_{L} with the lowest value of C. In this case, new vertices have to be computed.

Mathematically, the four possible transformations conditions for 2D simplex can be described as following. The multiplicative constants with conditions $\lambda > 0$, $0 < \kappa > 1$, $\tau > 1 \ \wedge \ \tau > \lambda$, $0 < \chi > 1$ used as parameters in these transformations equal $\lambda = 1$, $\kappa = \frac{1}{2}$, $\tau = 2$, $\chi = \frac{1}{3}$ in most of the implementations.

Step 1:

Reflection $\rightarrow$ compute the reflection point $V_{\mathrm{R}} = c + \lambda * (c - V_{\mathrm{H}})$ and tests a condition $C_{\mathrm{L}} \leq C_{\mathrm{R}} < C_{\mathrm{M}}$. If the result is true, accept the new simplex $V_{\mathrm{L}} V_{\mathrm{R}} V_{\mathrm{M}}$ and terminate the iteration.

Step 2:

if $C_{\mathrm{R}} < C_{\mathrm{L}}$:

Expansion $\rightarrow$ compute the expansion point $V_{\mathrm{E}} = c + \tau * (V_{\mathrm{R}} - c)$ and test a condition $C_{\mathrm{E}} \leq C_{\mathrm{R}} < C_{\mathrm{L}}$. If the result is true, accept the new simplex $V_{\mathrm{L}} V_{\mathrm{E}} V_{\mathrm{M}}$ and terminate the iteration, otherwise if false, accept the simplex $V_{\mathrm{L}} V_{\mathrm{R}} V_{\mathrm{M}}$ from previous step and terminate the iteration.

else if $C_{\mathrm{R}} < C_{\mathrm{M}}$:

Contraction $\rightarrow$ compute the contraction point V_{C}. If $C_{\mathrm{R}} < C_{\mathrm{H}}$, create the $V_{\mathrm{C}} = c + \kappa * (V_{\mathrm{R}} - c)$ outside the simplex and test a condition $C_{\mathrm{C}} < C_{\mathrm{R}}$. If the result is true, accept the new simplex $V_{\mathrm{L}} V_{\mathrm{C}} V_{\mathrm{M}}$ and terminate the iteration, otherwise if false, perform the Shrink operation. If $C_{\mathrm{H}} \leq C_{\mathrm{R}}$, create the $V_{\mathrm{C}} = c + \kappa * (V_{\mathrm{H}} - c)$ inside the simplex and test a condition $C_{\mathrm{C}} < C_{\mathrm{H}}$. If the result is true, accept the new simplex $V_{\mathrm{L}} V_{\mathrm{C}} V_{\mathrm{M}}$ and terminate the iteration, otherwise if false, perform the Shrink operation.

else:

Shrink computes N new vertices, $V_j = V_{\mathrm{L}} + \chi * (V_j - V_{\mathrm{L}})$ for $j \in \{0,...,N\}$ and $j \neq \mathrm{L}$ and accepts the new triangle $V_{\mathrm{L}} V_j$.
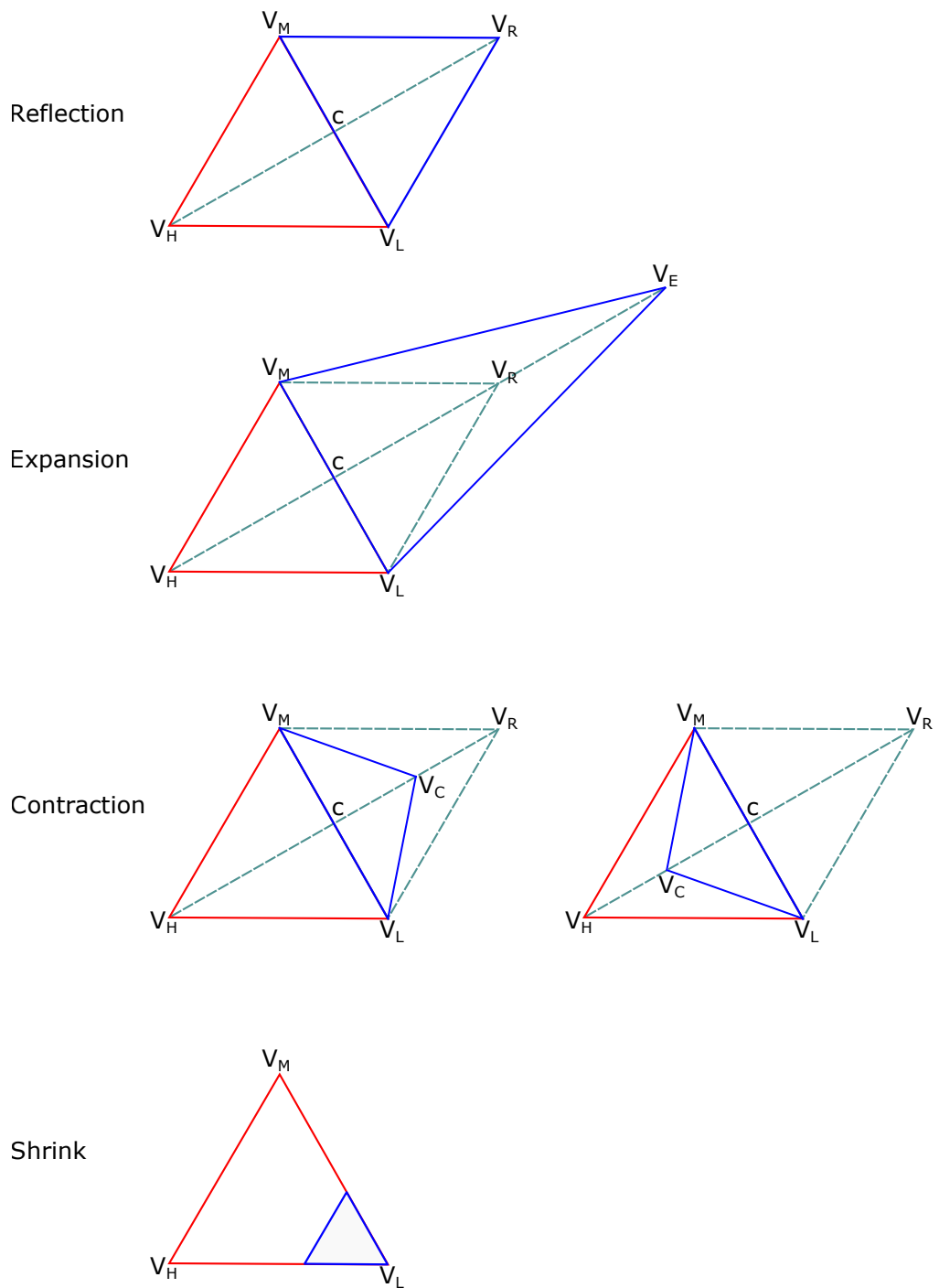
Figure 1.4: Nelder-Mead simplex transformations in 2D in following order: 1) Reflection, 2) Expansion, 3) Contraction and 4) Shrink.

Chapter 2

Construction and stability of the experimental setup

Parts of the text adopted from *Jan Jašek, Kateřina Jiráková, Karol Bartkiewicz, Antonín Černoch, Tomáš Fürst and Karel Lemr, Optics Express*, vol. 27, p. 32454, oct 2019 [1].

In previous chapter, we have described the basic theoretical concepts of quantum cloning and quantum information processing. We have also highlighted linear optics as a suitable platform for manipulating qubits encoded into photons and introduced machine learning as a viable methods of algorithmic optimization. In the experimental section, we will merge these concepts together to create a linear-optical quantum gate and show how to optimize it using reinforcement learning methods performed by classical information processing. Conceptually, this problem belongs to the QC class of reinforced quantum machine learning, which is visualized in Fig. 2.1.
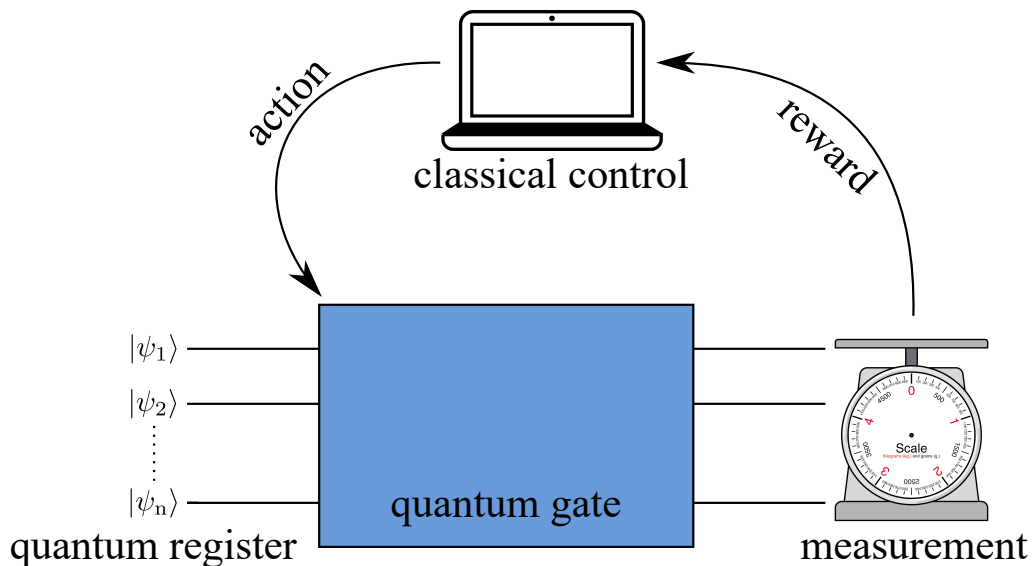
Figure 2.1: Conceptual scheme of hybrid reinforcement learning of quantum gate driven by classical control. In single iteration of the learning process, the control imposes action on the quantum gate, which alters the state of qubits in quantum register. The state of the qubits is then measured and used to evaluate the reward for the action, that is provided back to the classical control.

For our experiment, we chose to optimize the process of symmetrical $1 \rightarrow 2$
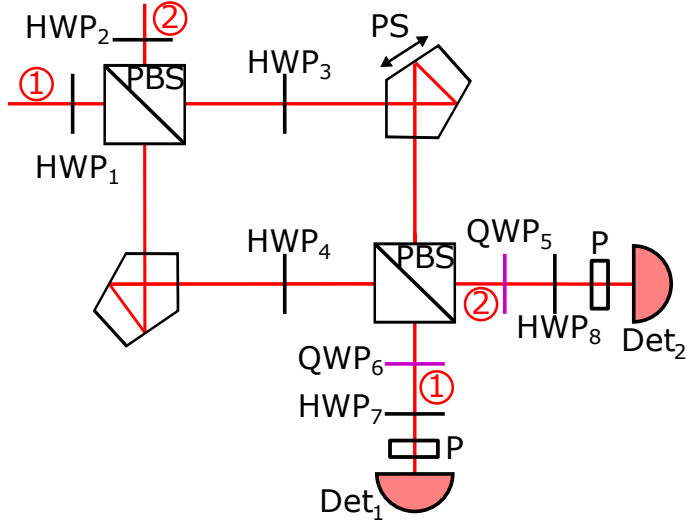
Figure 2.2: Scheme of built Mach-Zehnder interferometer. Legend: PBS – polarization beam splitter, PS – piezoelectric stage, HWP – half-wave plate, QWP – quarter-wave plate, Det – detector, P – polarizer. For measuring stability, the power meters were used as detectors. During cloning experiments, we detected single photons using avalanche photodiodes running in Geiger mode. Spatial modes are denoted by numbers.

phase-covariant quantum cloning discussed in Section 1.6.3, which is simple to realize and has known optimal results. The usual approach in quantum cloning is to explicitly derive the optimal (maximizing the output clones fidelities) cloning transformation of the system in particular quantum state, and then set the parameters of the experimental setup accordingly to perform such a transformation. In our case, however, we show that these parameters can be self-learned by the quantum cloner, provided the feedback based on the prior output clones fidelities.

2.1 Construction and stability of the interferometer, the core part of the experimental setup

There are many ways to realize a quantum cloner on the linear-optical platform. For our purposes, we built the device as a bulk type (i.e. the photon beams propagate in free space rather than optical fibers) Mach-Zehnder interferometer, which consists of two polarizing beam splitters (PBS) and two reflective pentaprisms, that can be seen in Fig. 2.2. One of the pentaprisms is attached to piezoelectric stage (PS). Apart from the interferometer, the experimental setup also included pairs of single mode optical fibers, decouplers (representing two input spatial modes) and couplers (representing two output spatial modes) and polarizers set to transmit only horizontally polarized modes. There are also eight wave plates in total, two quarter-wave plates (QWPs) and six half-wave plates (HWPs), which are described in detail in Section 2.2. The bulk type interferometer is convenient to use, as using fiber interferometer makes polarization states of the photons very difficult to control.

In order to successfully perform quantum cloning, the trasnformation performed on the input states has to be coherent and one of the most illustrative ways to prove coherence is interference. For observing interference, we have to ensure that both arms (paths of the optical signal) of the interferometer (spatial
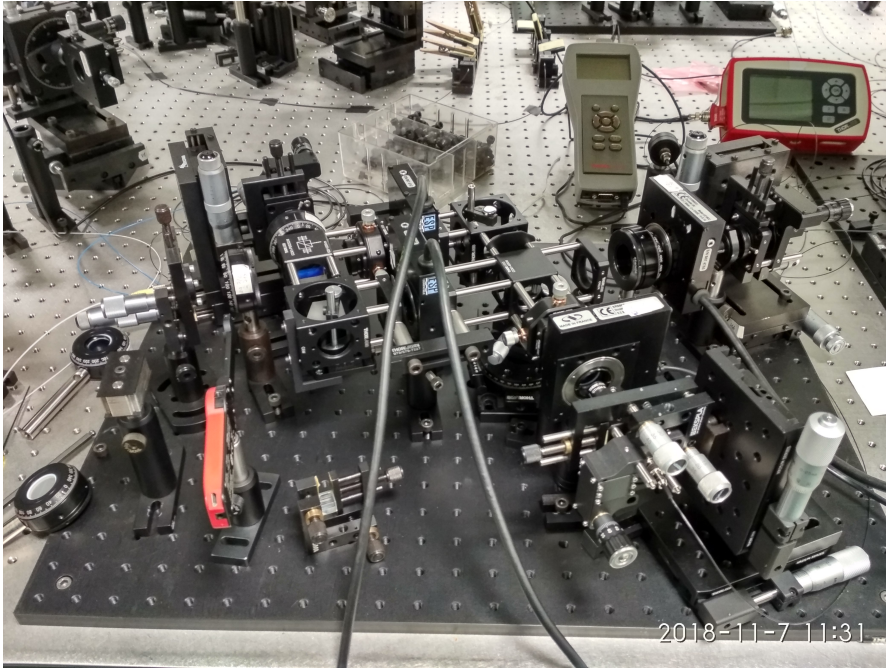
Figure 2.3: The ongoing construction of the experimental setup

modes 1 and 2) are equal in length, or rather that the temporal delay of photons in both modes equals. Moreover, we need to control the gate components with great precision, as the width of the core of single mode optical fiber is only $5\,\mu m$. Coupling and decoupling of the optical signal in such small dimensions can be done using precise translation and rotation stages.

In our case, couplers and decouplers can be both translated and rotated in two dimensions, which gives us four degrees of freedom, five in the combination with variable focusing distance of the coupler lenses. The pentaprisms also have to be mobile, one is tiltable in single dimension and the other one can be translated in one direction using movable piezoelectric stage (denoted by the arrow). Right PBS is also movable and is able to rotate in two dimensions a translate in one dimension.

Combining all of these components together allows us to equalize the photons temporal delay and couple the optical signal with high efficiency, although the process of configuring the whole interferometer is rather time consuming. To ensure maximum possible stability of the used components, we used a supporting cage system to reinforce the setup and bind the components together, as seen in Fig. 2.3. The figure shows work-in-progress experimental realization of the interferometer setup proposed above.

Ensuring that the temporal delay of photons in both spatial modes remains equal requires the interferometer to be highly stable. In this regard, we can distinguish two types of stability, construction stability, i.e. interferometer is stable in a sense of invariant indistinguishability of interfering modes, and phase stability, which can be interpreted as fine temporal stability of the interference of single input mode split at the first beam splitter.

In order to observe and quantify construction stability of the interferometer, i.e. whether the arms of the interferometer remain aligned, we can use visibility V. Visibility is an important parameter which quantifies the contrast of interference
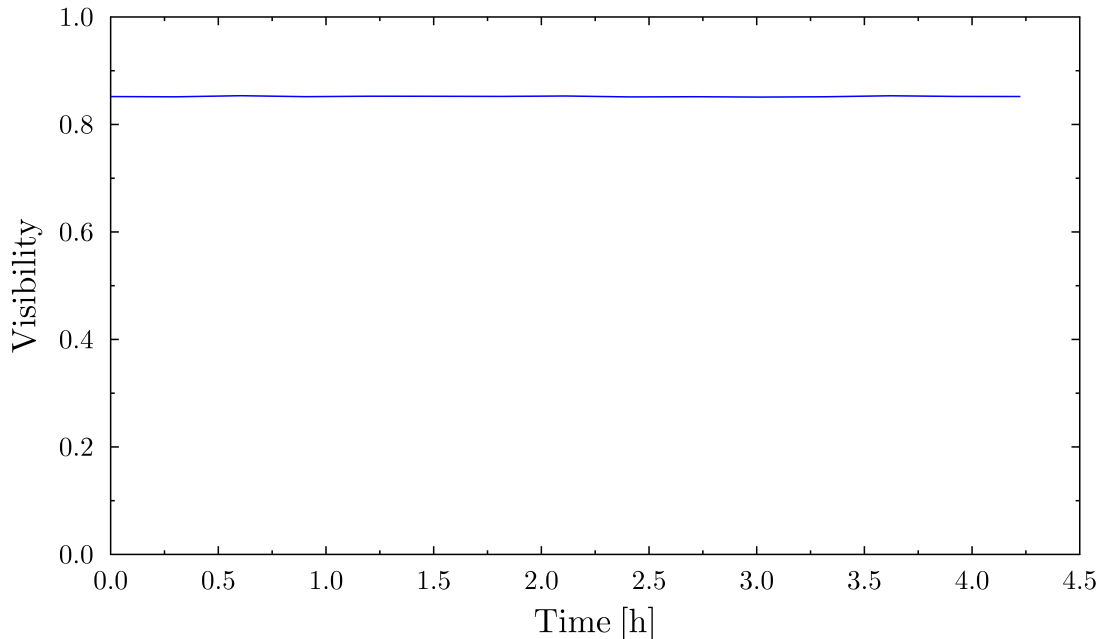
Figure 2.4: Visibility of the interferometer observed over 4 hours.

and is defined as

$$V = \frac{I_{\text{Max}} - I_{\text{Min}}}{I_{\text{Max}} + I_{\text{Min}}}, \tag{2.1}$$

where I_{Max} and I_{Min} stand for maximum and minimum signal intensity measured respectively while changing the optical path difference of the interferometer arms from zero to whole wavelength. For an ideally coherent light, $V = 1$, in real case scenarios (due to the experimental imperfections), we measure a number that is always lower.

We measured V as time dependent function of optical intensity from a testing laser beam at wavelength $\lambda = 695$ nm. Each realization of measuring V consisted of changing the voltage applied on the piezoelectric stage from -2.0 V to 2.0 V with step 0.1 V. This allowed us to scan the full interferometric fringe (including both the point of destructive interference and the point of constructive interference) and thus locate I_{Max} and I_{Min} needed for computing V.

For detection, we used power meters Thorlabs PM100 + S120B and PM100D + S151C. The measured visibility of our interferometer is plotted in Fig. 2.4. As we can see, with the use of reinforced setup construction, the visibility maintained a stable value around $V = 0.85$ for approximately four hours. The measured value of V is rather low during the setup construction as the perfect alignment of the setup wasn't required, because we used a testing laser beam at different wavelength than the single photon input later used for the cloning itself. Note that during the cloning process itself, visibility (more precisely, SPDC signal-photon visibility when detection is triggered by SPDC idler) was measured to be $V = 94.1 \pm 0.6$ %.

Ensuring that the construction of the interferometer is stable, we can observe the interference and quantify phase stability. Phase stability can be quantified by measuring a rate of change of optical intensity in selected period of time. As time progresses, fluctuations in temperature and elasticity of the material cause the components of the device to modify their mutual position, which actually
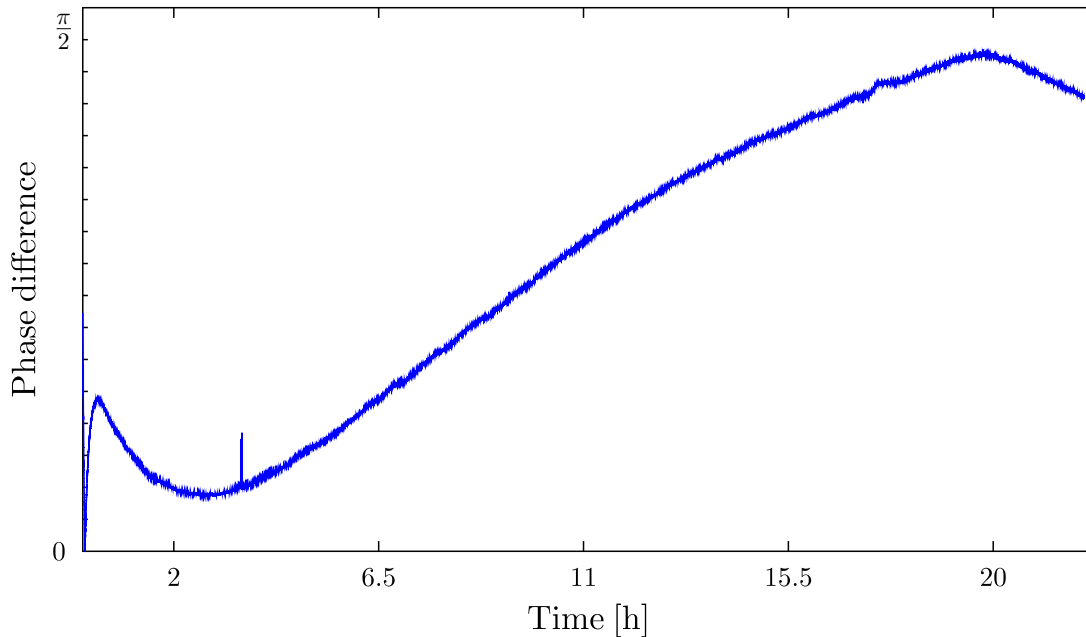
31

Figure 2.5: The original (passive) stability of the interferometer. Value 0 indicates minimal phase difference and thus constructive interference and value $\frac{\pi}{2}$ indicates point of maximal phase difference and destructive interference.

changes the photons temporal delay. That leads to the shift of phase difference between the optical signal in each path, which changes the interference and thus measured optical intensity.

As can be seen in Fig. 2.5, while the measurement started at the point of constructive interference (zero phase difference) on Det_2, the phase difference between the optical paths slowly changed close to a point of destructive interference (phase difference $\frac{\pi}{2}$) after approximately 16 hours. The corresponding optical path distance of the shift equals to the half of the wavelength of used laser beam. The initial rapid fluctuation was probably caused by the vibrations induced by movement in the laboratory.

For this measurement, we set HWP_2 to 22.5° and HWP_8 to the value corresponding to orthogonal state with respect to the required input signal state on HWP_2. All other HWPs were set to 0°, both QWPs to 45° and a minimum in single-input interference detections on Det_2 was found by tuning the voltage applied to PS (see Fig. 2.6). Note that for the measurement of phase stability, we only used the spatial mode 2 and measure optical intensity on Det_2.

To increase the stability of the interference, we used piezoelectric stage controlled by active stabilization algorithm, which used a parabolic curve fit of the function of signal in order to localize the minimum of the signal with increased precision and then moved the stage to that point of the minimum. Every tenth run, the algorithm also measured visibility V of the interferometer. Part of our Python implementation of the active stabilization can be seen in Source code 2.1. Our main focus here was to find out how often do we have to stabilize the interferometer in order to maintain phase and observe the interference.
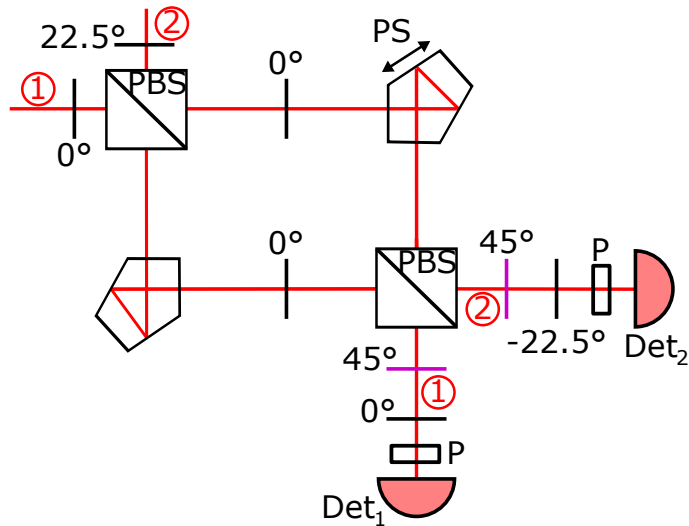
Figure 2.6: The configuration of experimental setup used for phase stabilization. Angles denote the specific configuration of wave plates used in Fig. 2.2 (QWPs are highlighted in purple color). Legend: PBS – polarization beam splitter, PS – piezoelectric stage, Det – detector, P – polarizer. Spatial modes are denoted by numbers. For measuring stability, the power meters were used as detectors. During cloning experiments, we detected single photons using avalanche photodiodes running in Geiger mode. Note that for the phase stability measurement, we only use the spatial mode 2.

```
1  def check (center, step):
2      k = 0
3      p = [0,0,0]
4      for i in [center-step, center, center+step]:
5          mujepcd.setVoltage(i)
6          temp = dev.getPower()
7          mujepcd.clear()
8          p[k]=temp
9          print(i,p[k])
10         k = k + 1
11     return p
12
13 def my_range(start, end, step):
14     while start <= end:
15         yield start
16         start += step
17
18 def minmax():
19     V = ""
20     min = 1000
21     max = 0
22     for f in my_range(-2,2,0.1):
23         mujepcd.setVoltage(f)
24         temp = dev.getPower()
25         mujepcd.clear()
26         if(temp > max):
27             max = temp
28         if(temp < min):
29             min = temp
30     vis = (max-min)/(max+min)
31     V = str(max) + "\t" + str(min) + "\t" + str(vis) + "\n"
32
33 dev = pm100d(options.port, False)
```

```
34  mujepcd = epcd ( options . epcdPort ,  options . defaultChannel ,  True ,  False
      )
35
36  step = 0.2
37  center = 0
38  p = [0 ,0 ,0]
39  P = 1000
40  i = 0
41  lastPower = −1
42
43  while True :
44    temp = dev . getPower ()
45    i = i + 1
46    if ( i %10 == 0 ) :
47      minmax ()
48    while True :
49      if ( center−step < −5):
50        center = 0
51      if ( center+step > 5 ) :
52        center = 0
53      p = check ( center , step )
54
55      if ( p [ 1 ] < p [ 0 ] and p [ 1 ] < p [ 2 ] ) :
56        print ( "Success?" ,p )
57        break
58      elif ( p [ 0 ] < p [ 1 ] and p [ 0 ] < p [ 2 ] ) :
59        center = center − step
60      else :
61        center = center + step
62
63    x1 = center−step
64    x2 = center
65    x3 = center+step
66    y1 = p [ 0 ]
67    y2 = p [ 1 ]
68    y3 = p [ 2 ]
69    denom = ( x1 − x2 )∗( x1 − x3 )∗( x2 − x3 )
70    A = ( x3 ∗ ( y2 − y1 ) + x2 ∗ ( y1 − y3 ) + x1 ∗ ( y3 − y2 ) ) / denom
71    B = ( x3 ∗∗2 ∗ ( y1 − y2 ) + x2 ∗∗2 ∗ ( y3 − y1 ) + x1 ∗∗2 ∗ ( y2 − y3 ) ) /
      denom
72
73    center = −B / (2∗A ) ;
74    mujepcd . setVoltage ( center )
75    lastPower = dev . getPower ()
76    mujepcd . clear ()
```

Source code 2.1: Implementation of the parabolic curve fit active stabilization loop

We ran five measurements in total, each with different repetition rate of the
stabilization algorithm. Resulting stability can be seen in Figs. 2.7, 2.8, 2.9, 2.10,
2.11 which actually represent a histogram of the frequency of specific optical path
deviations from default position in between two stabilizations. Rather than us-
ing units corresponding to the translation in length, we used distance expressed
in unit fractions of wavelength to emphasize how much has the optical paths
changed with respect to the used laser beam wavelength. As one can expect, we
can see that as the frequency of stabilization decreases, the higher mean wave-
length fraction (and thus higher temporal delay between photons) we measure.
For the last two measurements, we installed motorized half-wave plates into the

Table 2.1: Summary of active stabilization phase stability measurement. The asterisk (*) indicates usage of motorized components inducing mechanical vibrations. WF denoted wavelength and confidenal interval (Conf. interval) shows the range of 66.67% values around the median. The 8th (9th) decils indicates the worst value (i.e. the highest wave fraction) after subtracting worst 20% (10%) respectively.

Time period [s]	Median WF [m]	Conf. interval		8th decil	9th decil
10	$\frac{\lambda}{146.8}$	$\frac{\lambda}{92.3}$	$\frac{\lambda}{285.7}$	$\frac{\lambda}{97.2}$	$\frac{\lambda}{81.3}$
100	$\frac{\lambda}{170.7}$	$\frac{\lambda}{112.9}$	$\frac{\lambda}{360.2}$	$\frac{\lambda}{116.6}$	$\frac{\lambda}{95.3}$
1000	$\frac{\lambda}{58.4}$	$\frac{\lambda}{49.7}$	$\frac{\lambda}{67.1}$	$\frac{\lambda}{51.1}$	$\frac{\lambda}{37.7}$
30*	$\frac{\lambda}{76.1}$	$\frac{\lambda}{61.33}$	$\frac{\lambda}{85.1}$	$\frac{\lambda}{62.5}$	$\frac{\lambda}{50.5}$
300*	$\frac{\lambda}{64.8}$	$\frac{\lambda}{62.3}$	$\frac{\lambda}{70}$	$\frac{\lambda}{62.3}$	$\frac{\lambda}{53.7}$

interferometer, and measured the influence of rotating parts on the phase stability. Note that the motorized wave plates did not affect the polarization state of the propagating beam, they were used only to simulate the effect of mechanical vibrations.

A subplot on the right side of the figures represents the time function of relative voltage applied on the piezoelectric stage, which illustrates needed voltage difference to keep the phase stable. The scale of the voltage is recalculated to full wave units so that value 1 corresponds to a movement of piezoelectric stage of a whole wavelength. In other words, applying one unit to the piezoelectric stage changes the optical path length by the value of whole wavelength. We can see that the applied voltage increased more rapidly in the last two figures, with the motorized half-wave plates installed.

We can summarize resulting stability in Table 2.1. The table shows the time period between each stabilization, median wave fraction of the data as well as the values of 66.7% confidence interval and 8th and 9th decils. The confidence interval shows the range of 66.67% values around the median and the values of 8th (9th) decils indicates the worst value (i.e. the highest wave fraction) after subtracting worst 20% (10%) respectively. Curiously, the lowest mean wave fraction was achieved in second measurement with stabilization period 100 s, which is probably caused by the imperfect operation of piezo shift if the voltage is frequently changed, or by the effects of surrounding environment.

The asterisk in the last two lines indicates the measurement with used motorized components and we can clearly see, that there is a substantial increase in the mean wave length fraction. The motorized components thus have a significant impact on the phase stability.
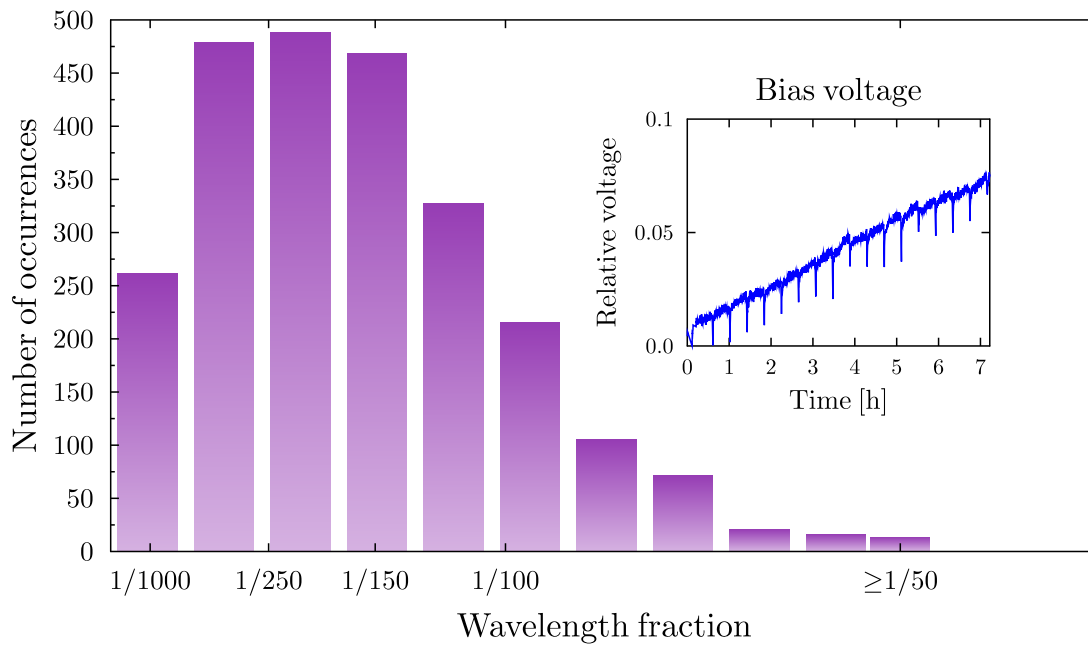
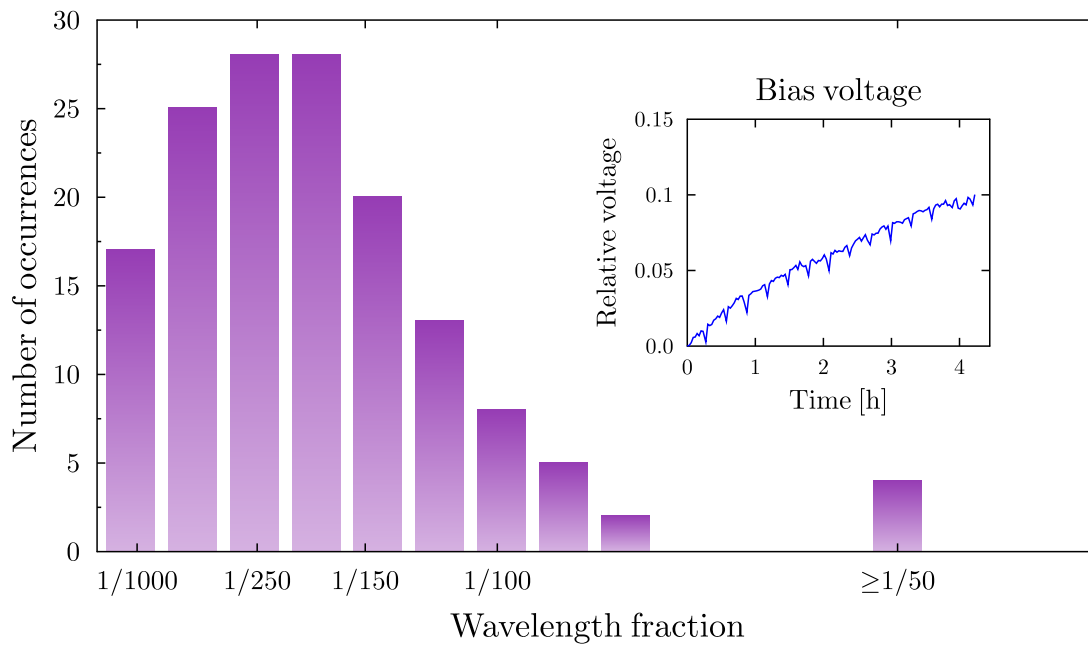Figure 2.7: The interferometer stability with active stabilization used with period $T = 10$ s

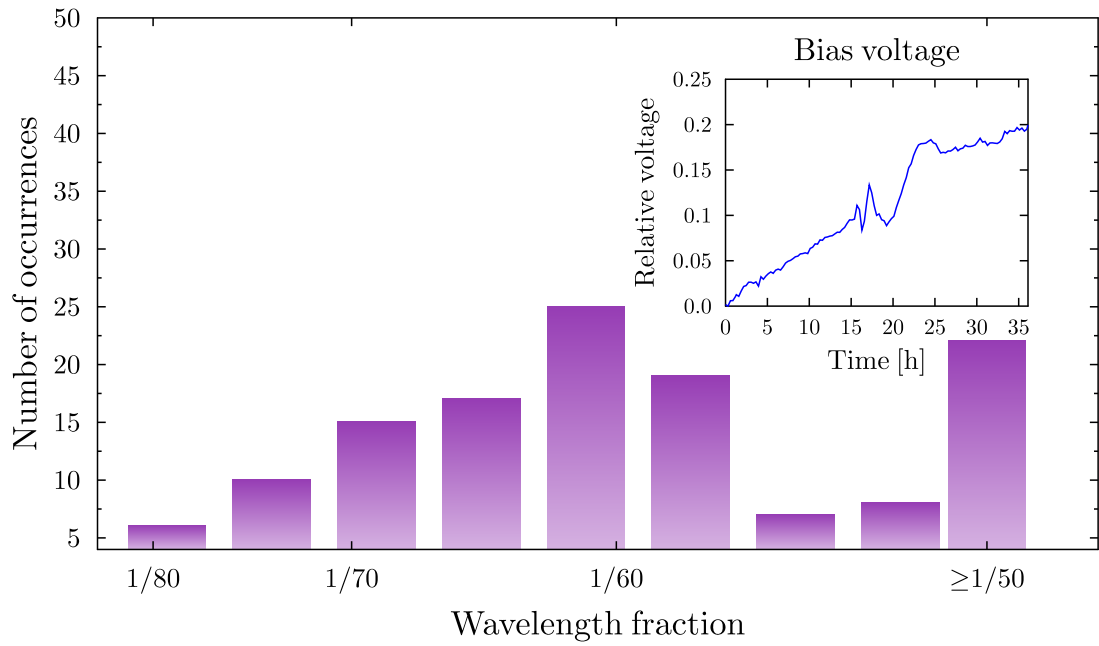Figure 2.8: The interferometer stability with active stabilization used with period $T = 100$ s

Figure 2.9: The interferometer stability with active stabilization used with period $T = 1000$ s
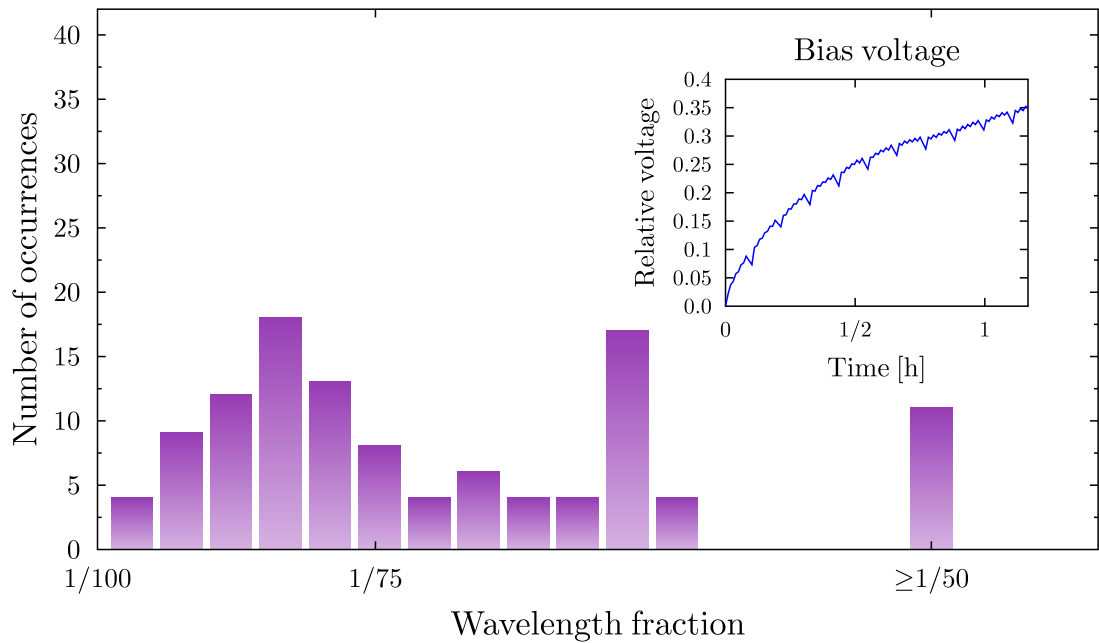

Figure 2.10: The interferometer stability with active stabilization used with period $T = 30$ s measured while rotation stage was moving.
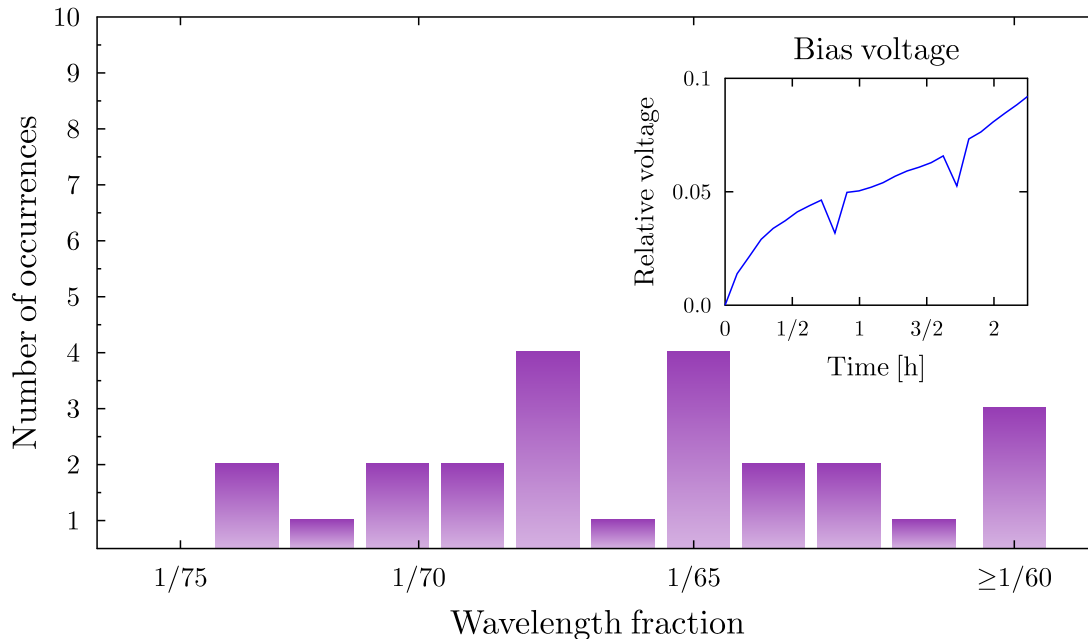
Figure 2.11: The interferometer stability with active stabilization used with period $T = 300$ s measured while rotation stage was moving.

2.2 Completion of the experimental setup and two photon interference

In the last section, we have described construction of Mach-Zehnder interferometer using linear-optical elements and then secured its phase stabilization using an active algorithm running on a classical computer. In this section, we insert a SPDC generated individual photon pairs as optical input of the quantum gate. The SPDC signal photon sets the input state of the qubit [see Eq. (1.42)], while the SPDC idler serves as the ancilla. In order to manipulate and clone the states, we also need to add active optical elements (motorized wave plates) which are controllable by computer, with respective angles ω, ϕ, θ serving as parameters for the cloning transformation.

The experimental setup is depicted in Fig. 2.12. The core part of the presented quantum gate is a Mach-Zehnder-type interferometer presented in section 2.1 which consists of two polarizing beam splitters and two reflective pentaprisms, one of which is attached to the piezoelectric stage. Pairs of photons are generated in Type I spontaneous parametric down-conversion occurring in a nonlinear BBO crystal. This crystal is pumped by Coherent Paladin Nd-YAG laser with integrated third harmonic generation at $\lambda = 355$ nm. The generated pairs of photons are both horizontally polarized and highly correlated in time. The temporal delay between photons of the pair can be adjusted using motorized translation stage (MT).

These photons are then spectrally filtered by 10 nm wide interference filters and spatially filtered by two single mode-optical fibers each guiding one photon of the pair. In our experimental setup, qubits are encoded into polarization states of individual photons ($|0\rangle \leftrightarrow |H\rangle$ and $|1\rangle \leftrightarrow |V\rangle$). The photon in the upper path (spatial mode 2) represents the signal qubit, quantum state of which we want to clone, and the photon in the lower path (spatial mode 1) serves as the ancilla,
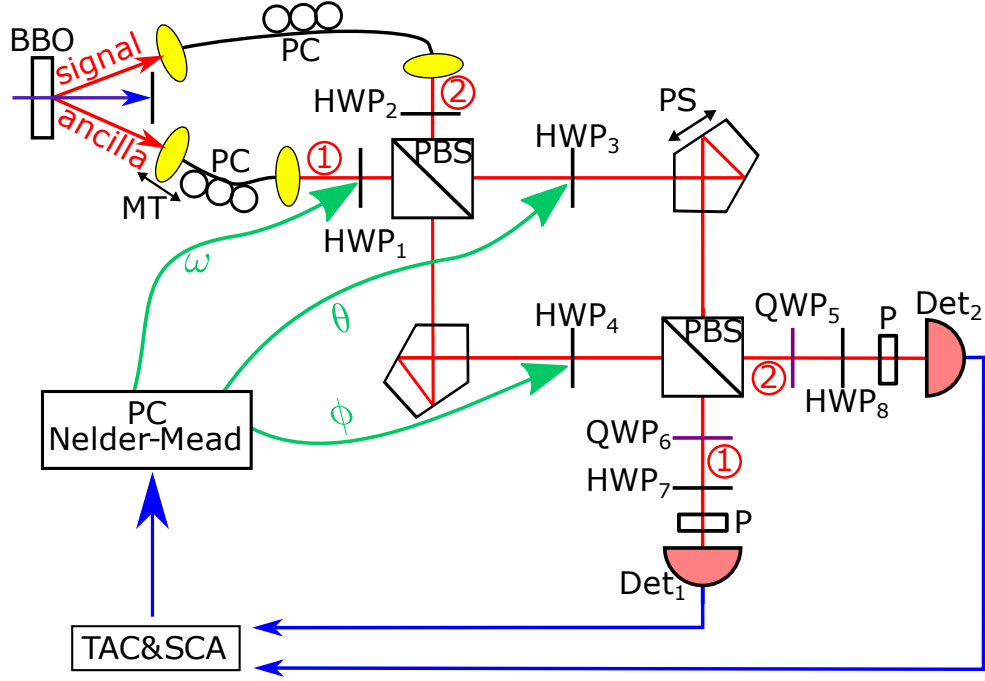
Figure 2.12: Experimental setup. Legend: PBS – polarization beam splitter, PC – polarization controller, BBO – barium beta borate, Det – detector, HWP – half-wave plate, QWP – quarter-wave plate, MT – motorized translation stage, PS – piezoelectric stage, TAC&SCA – time-to-amplitude converter & single channel analyzer. Spatial modes are denoted by numbers.

the state of which reads

$$|\psi_{\mathrm{a}}\rangle = \cos\left(2\omega\right)|H\rangle + \sin\left(2\omega\right)|V\rangle \ . \tag{2.2}$$

The parameter ω is controlled by the rotation of HWP_1 (see Fig. 2.12).

Using polarization controllers (PC) we can ensure that both photons are horizontally polarized at the output of the fibers. From now on, polarization states of the photons are set using a combination of half-wave plates (HWPs) and quarter-wave plates (QWPs). There are eight wave plates in total, two stationary QWPs fixed at angle 45°[1] and six motorized HWPs which make it possible to control the whole quantum gate using a computer.

The first two half-wave plates HWP_1 and HWP_2 are used to set input polarization states of the ancilla and cloned photons, respectively. With the addition of two HWPs (HWP_3 and HWP_4) placed in its arms, this whole interferometer implements a polarization dependent beam splitter with variable splitting ratio. Mathematically, the transformation matrix of the gate reads

---

[1]All mentioned angles of wave plates are angles between the wave plates optical axis and horizontal plane.

$$
\begin{pmatrix} \hat{a}_{\mathrm{Hout},1} \\ \hat{a}_{\mathrm{Vout},1} \\ \hat{a}_{\mathrm{Hout},2} \\ \hat{a}_{\mathrm{Vout},2} \end{pmatrix} = M_{\mathrm{bias}} \times M_{\mathrm{PBS}} \times M_{\theta\phi} \times M_{\mathrm{PBS}} \times M_{\mathrm{bias}} \begin{pmatrix} \hat{a}_{\mathrm{Hin},1} \\ \hat{a}_{\mathrm{Vin},1} \\ \hat{a}_{\mathrm{Hin},2} \\ \hat{a}_{\mathrm{Vin},2} \end{pmatrix}
$$

$$
= \begin{pmatrix} \cos(2\phi) & 0 & \sin(2\phi) & 0 \\ 0 & \cos(2\theta) & 0 & \sin(2\theta) \\ -\sin(2\phi) & 0 & \cos(2\phi) & 0 \\ 0 & -\sin(2\theta) & 0 & \cos(2\theta) \end{pmatrix} \begin{pmatrix} \hat{a}_{\mathrm{Hin},1} \\ \hat{a}_{\mathrm{Vin},1} \\ \hat{a}_{\mathrm{Hin},2} \\ \hat{a}_{\mathrm{Vin},2} \end{pmatrix}
$$

(2.3)

where $\hat{a}_{x,i}$ represents the annihilation operators of the individual input, polarization ($x \in \{H,V\}$) as well as spatial ($i \in \{1,2\}$) modes. In the matrix product (2.3), the matrix

$$
M_{\mathrm{PBS}} = \begin{pmatrix} 1 & 0 & 0 & 0 \\ 0 & 0 & 0 & 1 \\ 0 & 0 & 1 & 0 \\ 0 & -1 & 0 & 0 \end{pmatrix}
$$

(2.4)

represents transformation of single polarizing beam splitter and the matrix

$$
M_{\theta\phi} = \begin{pmatrix} \cos(2\theta) & \sin(2\theta) & 0 & 0 \\ \sin(2\theta) & -\cos(2\theta) & 0 & \\ 0 & 0 & \cos(2\phi) & \sin(2\phi) \\ 0 & 0 & \sin(2\phi) & -\cos(2\phi) \end{pmatrix}
$$

(2.5)

represents the combination of HWP_3 and HWP_4, while angles θ and ϕ correspond to the rotations of HWP_3 and HWP_4. In order for the gate to be formally equivalent to the transformation by a polarization dependent beamsplitter [see Eq. (1.35)], one input and one output mode (spatial mode 1) needs to have their polarization modes swapped, effectively interchanging ($|H\rangle \leftrightarrow |V\rangle$). This is represented by the first and last matrix of the product,

$$
M_{\mathrm{bias}} = \begin{pmatrix} 0 & 1 & 0 & 0 \\ 1 & 0 & 0 & 0 \\ 0 & 0 & 1 & 0 \\ 0 & 0 & 0 & 1 \end{pmatrix},
$$

(2.6)

and experimentally implemented by adding a constant bias angle to rotations of HWP_1 and HWP_7. Intensity splitting ratios of such beam splitter for horizontal and vertical polarizations equal $\cot^2(2\phi)$ and $\cot^2(2\theta)$, respectively.

The two spatial modes at the output of the interferometer are subjected to polarization projection (QWP_5, QWP_6 and HWP_7, HWP_8) and then led via single-mode optical fibers to a pair of avalanche photodiodes COUNT NIR 100N by Laser Components running in Geiger mode. We use detection electronics to register both single photons at each of the detectors and coincident detections as successful operation of the gate is indicated by the presence of single photon in each output of the interferometer. The electronic signal is then sent to a classical computer.

Our next task is to minimize the temporal delay between the individual photons of the discrete pairs. To achieve this, all HWPs are set to[2] 0° with the

---

[2]Note that the bias of 45° applies to HWP_1 rendering its true rotation angle to 0° + 45° = 45°.
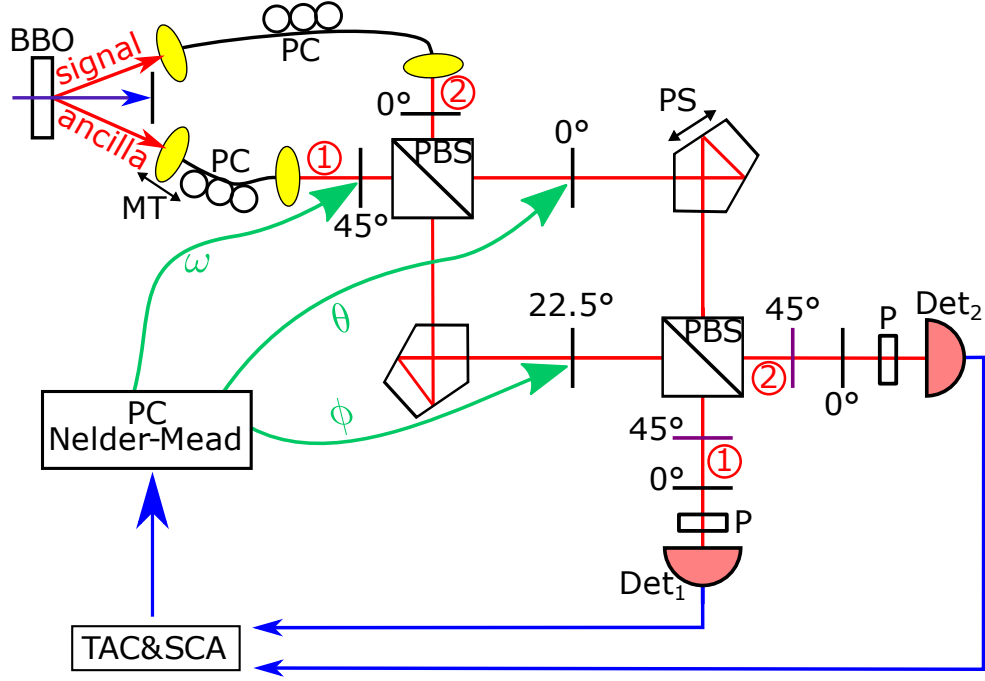
Figure 2.13: The configuration of experimental setup used for finding Hong-Ou-Mandel dip (two-photon interference). QWPs are highlighted in purple color. Legend: PBS – polarization beam splitter, PC – polarization controller, BBO – barium beta borate, Det – detector, PS – piezoelectric stage, TAC&SCA – time-to-amplitude converter & single channel analyzer. Spatial modes are denoted by numbers.

exception of HWP_4 being at 22.5° as can be seen in Fig. 2.13. In this regime, we minimize the number of two-photon coincident detections (Hong-Ou-Mandel dip [53]) by changing the temporal delay between the photons using a motorized translation stage MT.

By minimizing the temporal delay between photons, we observe their bunching on the HWP_4 which acts on the polarization modes like a balanced beam splitter on spatial modes. The coincident detection count as a function of relative position of MT in μm is expected as a product of Gaussian function and a sinc function [54]

$$cc(x) = b - a \, \exp\left(\frac{-4\ln(2)\,(x-c)^2}{w^2}\right)\left(\frac{\sin(f\,(x-c))}{f\,(x-c)}\right). \qquad (2.7)$$

The parameters of the fit were calculated as $a = 1910 \pm 70$, $b = 2000 \pm 40$, $c = 0.7 \pm 0.3$, $f = 0.105 \pm 0.005$, $w = 70 \pm 10$ can be seen in Fig. 2.14. The line segments of the individual measured points represents the Poisson noise uncertainty, which is equal to a square root of the measured value. Visibility of the measured dip equals $V = 92 \pm 4$ %.
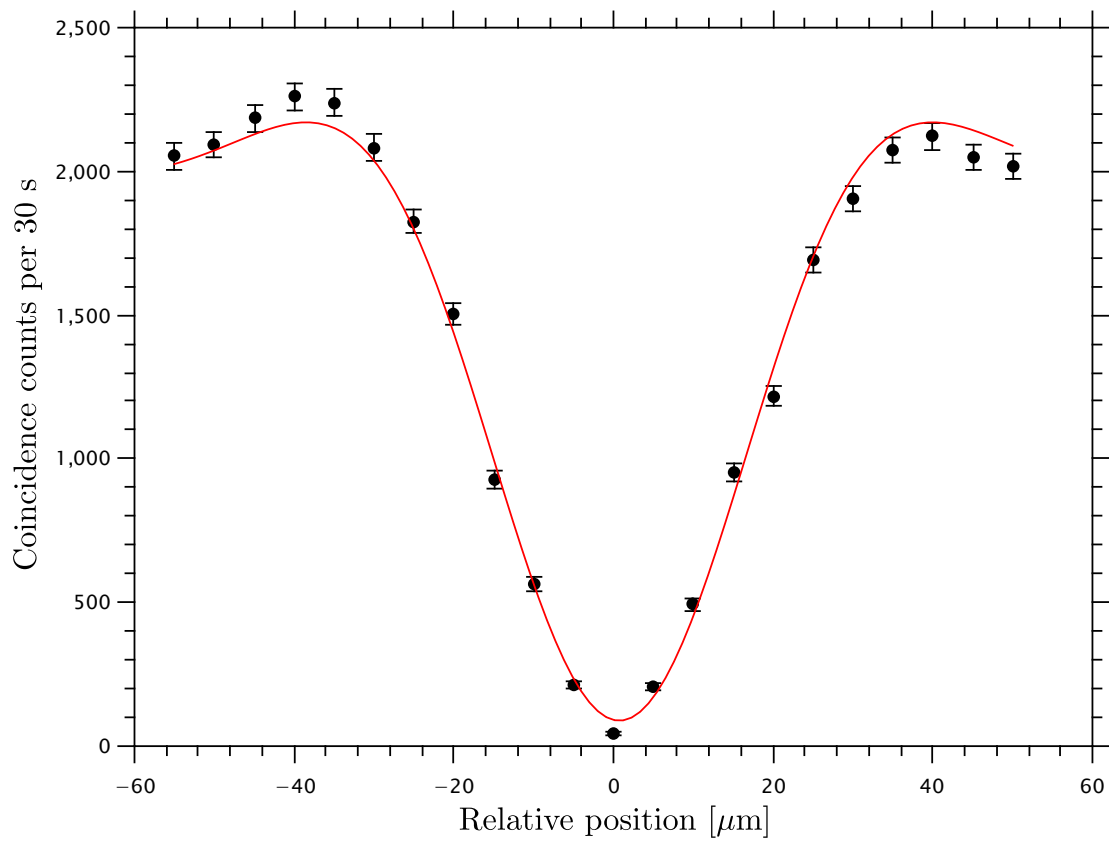
Figure 2.14: Measured two-photon interference (Hong Ou Mandel) dip with a curve fit of function 2.7.

Chapter 3

Experimental quantum cloner: algorithmization, training and results

Parts of the text adopted from *Jan Jašek, Kateřina Jiráková, Karol Bartkiewicz, Antonín Černoch, Tomáš Fürst and Karel Lemr, Optics Express*, vol. 27, p. 32454, oct 2019 [1].

In the previous section, we have completed the construction of a proposed linear optical quantum gate. Our next goal is to algorithmize the gate using classical information processing. While the gate itself is capable of a broad range of two qubit transformations, our focus was aimed on its ability to act as a phase-covariant quantum cloner. Its figure of merit is the individual fidelity of the output copies as defined in Section 1.6.1.

As mentioned before, the input quantum states will be limited to the class of Equatorial states [see Eq. (1.42)] and the maximal theoretical fidelity of clones of such states equals $F = \frac{1}{2}\left(1 + \frac{1}{\sqrt{2}}\right) \approx 0.8535$. In the best-case scenario, the cloner would achieve this fidelity after the learning is completed.

For specific parameters of the presented linear-optical elements, this quantum gate functions as a $1 \to 2$ symmetric phase-covariant cloner, optimal analytical cloning transformation of which is well known [40]. On a linear-optical platform, this optimal cloning transformation can be achieved by a polarization dependent beam splitter with intensity transmissivities for horizontal and vertical polarization at $T_{\mathrm{H}} \approx 0.21$ and $T_{\mathrm{V}} \approx 0.79$, while setting the ancilla to be horizontally polarized. Note that our quantum gate is capable of implementing this transformation when set approximately to $\phi = 31.3°$, $\theta = 13.7°$.

To showcase the capability of our gate to learn to clone phase-covariant states optimally, we deliberately ignore this analytical solution and employ self-optimization procedure seeking to maximize the cloning fidelities. The optimization process consists of a number of measurements (runs), each performed for a set of variable optimization parameters ϕ, θ, ω. That is, the variable splitting ratio for horizontal (ϕ) and vertical (θ) polarization as well as the state of the ancilla (ω). In each run, output clones fidelities are evaluated and supplied to the classical Nelder-Mead algorithm [46] for a decision about the parameters of future runs.

In between any two runs, the setup is stabilized. We first minimize temporal delay between the two individual photons as described in Section 2.2. In the

next step, the phase is stabilized in the interferometer in accordance with Section 2.1. Moreover, we make use of the fact that the phase shift in the interferometer additively contributes to the phase α of the signal state. This allows us to use interferometer phase stabilization for setting of any signal state of the equatorial class. Note that the entire stabilization procedure is completely independent of the learning process itself.

While all six of the HWPs are controlled by a PC, only three (HWP$_1$, HWP$_3$ and HWP$_4$) are specifically controlled by the optimization algorithm. In contrast to that, HWP$_2$ is used to set the quantum state of the cloned qubit and HWP$_7$ and HWP$_8$ are used to choose polarization projections, therefore their configuration shall not be accessible to the optimization algorithm.

In this reinforced-learning scenario, the cloner is trained on a sequence of random equatorial signal states (1.42) different for each run. The phase α is randomly picked from interval $[0; 2\pi[$. The optimization algorithm then rotates HWP$_1$, HWP$_3$ and HWP$_4$ to chosen angles ϕ, θ, ω. Finally, the cloner is fed back the measured fidelities F_1, F_2 of the first and second respective clones. The core part of the optimization process is the Nelder-Mead simplex algorithm described in Section 1.7.2 which minimizes a chosen cost function C. In our case, we defined the cost function C to maximize the obtained fidelities and simultaneously achieve symmetry of the cloning

$$ C = (1 - F_1)^2 + (1 - F_2)^2 + (F_1 - F_2)^2. \tag{3.1} $$

The fidelities are obtained by measuring coincidence detections in four different projection settings that correspond to the angles set on HWP$_7$ and HWP$_8$. We label these coincident detections cc_{ij}, where $i, j \in \{\|; \perp\}$. The $\|$ and the $\perp$ sign denote projection on the signal state $|\psi_\mathrm{s}\rangle$ and its orthogonal counterpart $|\psi_\mathrm{s}^\perp\rangle$. We calculate the fidelities as

$$ F_1 = \frac{cc_{\|\|} + cc_{\|\perp}}{\Sigma}, \ F_2 = \frac{cc_{\|\|} + cc_{\perp\|}}{\Sigma}, \tag{3.2} $$

where Σ denotes $cc_{\|\|} + cc_{\|\perp} + cc_{\perp\|} + cc_{\perp\perp}$.

In the previous section, we have also defined the transformatin matrix of the quantum gate as in Eq. (2.3). To simulate this transformation (and to create a theoretical reference to our experimental approach), we have implemented Python algorithm that can be seen in Source code 3.1

```
1  def sin(angle):
2      angle = angle * np.pi / 180
3      return np.sin(angle)
4
5  def cos(angle):
6      angle = angle * np.pi / 180
7      return np.cos(angle)
8
9  def fidelity(angles):
10     global alpha
11     global beta
12     global F1,F2
13     fi = angles[0]
14     theta = angles[1]
15     omega = angles[2]
16     #Creation of state describing ket
17     state = np.matrix([[alpha],[beta],[0],[0]])
```

```python
18
19        #Transformation matrix
20        mres = np.matrix([[complex(cos(2*omega)*cos(2*theta)*cos(2*fi),
       -1*sin(2*omega)*sin(2*theta)*sin(2*fi))/2**(1/2)],
21                          [complex(sin(2*omega)*cos(4*theta),0)/2**(1/2)],
22                          [complex(0,1*cos(2*omega)*cos(4*fi))/2**(1/2)],
23                          [complex(-1*cos(2*omega)*sin(2*theta)*sin(2*fi),
       1*sin(2*omega)*cos(2*fi)*cos(2*theta))/2**(1/2)]])
24
25        mrestr = np.matrix([[complex(cos(2*omega)*cos(2*theta)*cos(2*fi)
       , 1*sin(2*omega)*sin(2*theta)*sin(2*fi))/2**(1/2)],
26                          [complex(sin(2*omega)*cos(4*theta),0)/2**(1/2)],
27                          [complex(0,-1*cos(2*omega)*cos(4*fi))/2**(1/2)],
28                          [complex(-1*cos(2*omega)*sin(2*theta)*sin(2*fi)
       ,-1*sin(2*omega)*cos(2*fi)*cos(2*theta))/2**(1/2)]])
29
30        #Probability of success
31        pu = abs(mres[0])**2 + abs(mres[1])**2 + abs(mres[2])**2 + abs(
       mres[3])**2
32
33        #Density matrix
34        mro = np.dot(mres,np.transpose(mrestr))
35        mro = np.divide(mro,pu)
36
37        #Partial trace 1
38        mtr1 = mro[np.ix_([0,1],[0,1])] + mro[np.ix_([2,3],[2,3])]
39
40        #Fidelity 1
41        state = np.matrix([[alpha],[beta]])
42        statetr = np.matrix([[alpha],[-1*beta]])
43        temp = np.dot(np.transpose(statetr),mtr1)
44        Fid1 = np.dot(temp,state)
45
46        #Partial trace 2
47        mro[:,[1, 2]] = mro[:,[2, 1]]
48        mro[[1,2],:] = mro[[2,1],:]
49        mtr2 = mro[np.ix_([0,1],[0,1])] + mro[np.ix_([2,3],[2,3])]
50
51        #Fidelity 2
52        temp = np.dot(np.transpose(statetr),mtr2)
53        Fid2 = np.dot(temp,state)
54
55        F1 = np.real(Fid1)
56        F2 = np.real(Fid2)
57        pot = (F1-F2)**2 + (1-F1)**2 + (1-F2)**2
58
59        anglesMat.append([fi+45,theta+45,omega])
60        return pot
61
62 F1 = 0
63 F2 = 0
64 alpha = (1/2)**(1/2) # State
65 beta = complex(0,(1/2)**(1/2)) # State
66 fi = 0
67 theta = 0
68 omega = 22.5
69 angles = [fi, theta,omega]
70 anglesMat = []
```

```
71 initialSimplex = np.array ([[ fi ,theta ,omega ] ,[ fi −15,theta −15,omega
       +15] ,[ fi −15,theta ,omega ] ,[ fi ,theta −15,omega ]])
72
73 xopt = scipy.optimize.minimize ( fidelity , angles , method='Nelder−Mead' ,
       options={'initial_simplex ': initialSimplex , 'disp ':True , '
       return_all ':True })
```
Source code 3.1: Theoretical 3D model of quantum cloner implemented in Python.

3.1 Results

We have experimentally implemented two machine learning models using two and three parameters, respectively. We have also run computer simulations to both of the models to visualize and cross-reference theoretical optimum scenario.

In the first model, we fixed the ancillary state to one of its theoretically known optimum $|\psi_\mathrm{a}\rangle = |H\rangle$ (the parameter ω was therefore fixed at $\omega = 45°$). The remaining two parameters of the gate ϕ and θ were machine learned. To minimize the cost function (i.e. optimize the performance of the cloner) we applied Nelder-Mead simplex algorithm which iteratively searches for a minimum of a cost function [see Eq. (3.1)].

Training of the gate consists of providing it with training instances of equatorial qubit states (randomly generated in each cost function evaluation) and with the respective fidelity of the clones. In each training run, the underlying Nelder-Mead algorithm sets the gate parameters to initial vertices of simplexes in the parameter space and then decides on a future action.

In the case of a two-parameter optimization, these simplexes correspond to triangles and can be visualized onto a contour plot of the cost function, as depicted in Figure 3.1. In this Figure, we plot the exact path taken by the Nelder-Mead simplex algorithm to minimize the cost function C for the case of a real experiment (b) and its simulation (a). We can see that while the initial runs created almost identical simplexes, as the area of the simplex decreased, the experimentally measured simplexes started to deviate from its simulation. This is likely caused by the experimental error, such as Poisson noise and misalignment of the device. Note that the selected initial simplex was intentionally chosen well away from the optimal position – its first vertex resembles the trivial cloning strategy [55, 56].

In Figure 3.2 we illustrate the evolution of both the fidelities F_1, F_2 and the cost function C during the training for (a) the simulation and (b) experimental data. We can see that the convergence point was found more precisely in the simulation, but the resulting values of both simulated and experimentally learned fidelities and cost function match. After 40 runs (i.e. 40 instances from the training set), this model was deemed trained because the size of simplexes dropped to the experimental uncertainty level (i.e. $\sim$ 0,1° on rotation angles of wave plates). However, in general, setting the simplex to converge within a given precision is a nontrivial problem [57].

For the second model, we added third parameter and let the gate learn the optimal setting of the ancilla ω along with the gate parameters ϕ and θ. The training procedure ran identically to the first model, with notable difference that optimized simplexes had 3 vertices, which can't be clearly visualized in 2D plot.
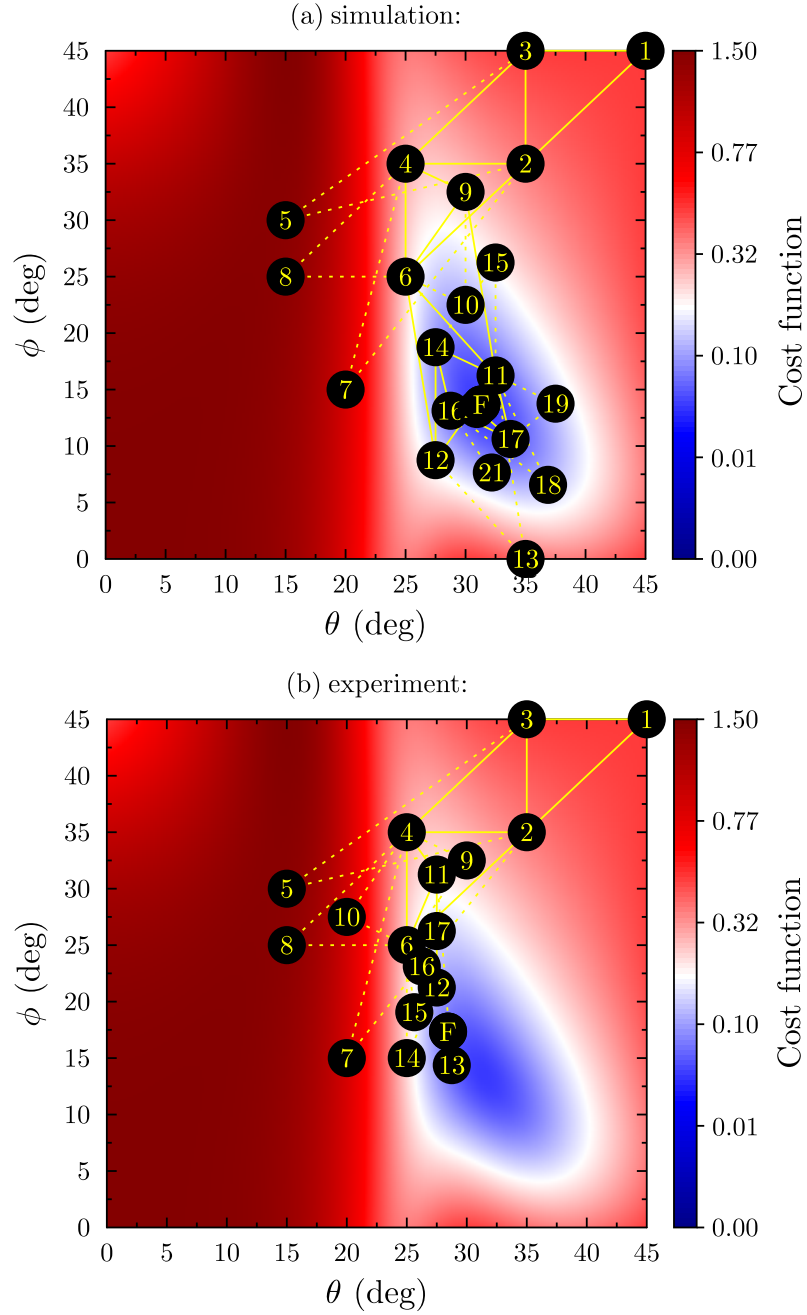
(a) simulation:

(b) experiment:

Figure 3.1: Contour plot of the cost function C for the angles ϕ and θ (corresponding to HWP_4 and HWP_3 in Figure 2.12, respectively). The solid yellow lines denote the final triangles reached by the Nelder–Mead simplex algorithm in each of its iteration. The dashed lines mark intermediate steps, which were rejected (see Fig. 1.4). The circled numbers stand for gate runs and point F depicts the final state of the gate at the end of training. A simulation was performed prior to the experiment to verify our implementation of the learning algorithm. Differences between the experimentally learned and simulated parameters can be explained by imperfections in the experimental setup. Author gratefully acknowledges Kateřina Jiráková, coauthor of the article [1], as the author of this Figure.
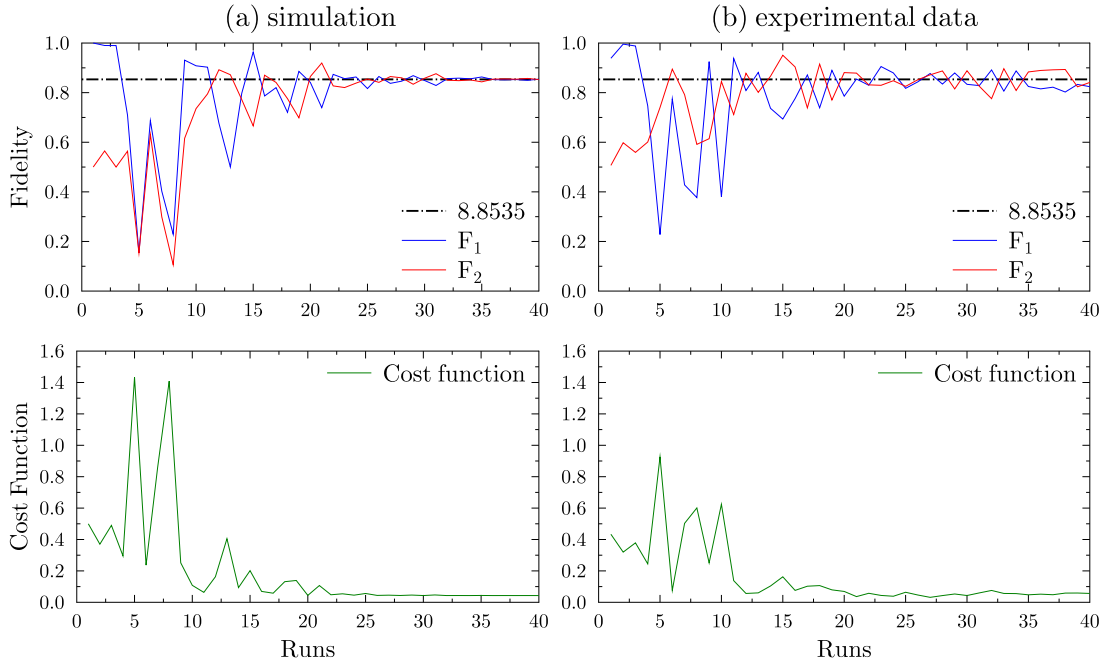
Figure 3.2: Plots showing the evolution of fidelity of both the clones (top) as well as the cost function (bottom) throughout the training in case of (a) simulation of the first model and (b) experimental data of the first model with two free parameters ϕ and θ. The thick dashed black line marks the theoretical optimum of achieved fidelity $F \approx 0.8535$. Fidelity of the first clone F_1 is visualized by a solid blue line and the fidelity of the second clone F_2 is shown in solid red line. The cost function C is indicated by solid green line.

The evolution plot of the measured fidelities F_1, F_2 and cost function C throughout the training of this three-parameter model can be seen in Fig. 3.3. We can see that while the experimentally measured plots are less smooth than its simulated counterparts, the final values of the fidelities match the theoretical optimum. The initial value of the ω parameter was set naively to $\omega = \frac{\pi}{8}$ so it lied on the equator of the Poincaré-Bloch sphere. Using a similar stopping criterion as in the first model, the training of the second model was terminated after 60 runs.

After the training procedure was completed, we have tested the performance of both our models on independent test sets each consisting of 40 instances of random equatorial states and summarized the results in Table 3.1. Table provides the final learned parameters together with the mean values of the fidelities on the test sets $\langle F_1 \rangle$ and $\langle F_2 \rangle$ for both simulated and experimental data.

The experimentally observed clone fidelities on test sets are bordering on the theoretical limit (at most 0.013 below it) which renders our gate highly precise in context of previously implemented cloners [40, 58–61]. Unlike the fidelities, the optimized parameteres ϕ, θ, ω converged to a different values than the simulation during the experimental training procedure. While the theoretically expected (simulated) values equal $\phi = 31.3°, \theta = 13.7°, \omega = 45°$, the first model yielded $\phi = 28,59°, \theta = 17.11°$ and the second model converged to the values $\phi = 27.44°, \theta = 21.68°, \omega = 41.49°$. This is likely caused by the imperfections of the experimental setup, especially the misalignment of the interferometer and imprecise setting of both each of the wave plates reference value (0°) and polarization controllers at the input of the setup.
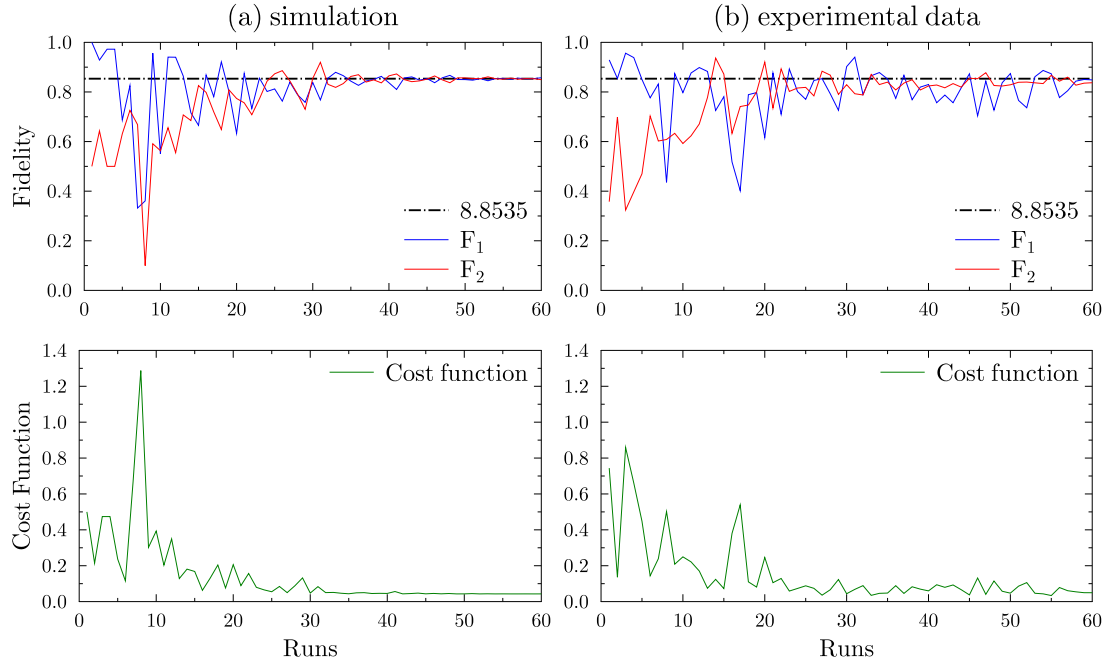
Figure 3.3: Plots showing the evolution of fidelity of both the clones (top) as well as the cost function (bottom) throughout the training in case of (a) the simulation of the second model and (b) experimental data of the second model with three free parameters ϕ, θ and ω. The thick dashed black line marks the theoretical limit of $F \approx 0.8535$. Fidelity of the first clone F_1 is visualized by a solid blue line and the fidelity of the second clone F_2 is shown in solid red line. The cost function C is indicated by solid green line.

Table 3.1: Summary of the final values for both models and their respective simulations. Angles ϕ, θ, ω show the final values of the optimized parameters after a number of training runs. Values $\langle F_1 \rangle$ and $\langle F_2 \rangle$ denote the mean fidelities observed on the independent test sets after the training of the cloner was completed.

Final values	Sim. 1	Sim. 2	Model 1	Model 2
training:				
Angle ϕ	31.31°	31.31°	28.59°	27.44°
Angle θ	13.68°	13.68°	17.11°	21.68°
Angle ω	45° (Fixed)	45°	45° (Fixed)	41.49°
No. of training instances (runs)	40	60	40	60
testing:				
$\langle F_1 \rangle$	0.854	0.854	0.840 ± 0.033	0.849 ± 0.040
$\langle F_2 \rangle$	0.854	0.854	0.843 ± 0.046	0.853 ± 0.022

Conclusions

In this thesis, we demonstrated reinforcement-learned quantum cloner for a class of phase-covariant quantum states, constructed as a two qubit gate on the platform of linear optics. The first chapter highlighted basic theoretical concepts and principles that are used in the fields of quantum optics, quantum information processing, quantum cloning and both classical and quantum machine learning. We also thoroughly described design of the Nelder–Mead simplex algorithm used in our work.

In the second chapter, we described the construction and stability characterization of the gate itself. The gate constitutes of several linear-optical elements, the core part of which is a bulk Mach-Zehnder-type interferometer. To ensure the coherence of the transformations performed by the gate and equalize temporal delay between photons propagating through the interferometer, we have realized several stability measurements, distinguishing the stability of construction and phase stability. The stability of construction was quantized using visibility V to the value $V = 94.1 \pm 0.6$ %. We also showed that visibility maintained a stable value over the course of four hours.

For the phase stability, we measured optical intensity of interference between the photons of single input mode split at the beam splitter. The phase difference between the photons slowly changed from 0 to $\frac{\pi}{2}$ over the course of 16 hours. In order to improve the phase stability, we have successfully implemented an active stabilization algorithm that applied voltage to a piezoelectric stage. The algorithm located the minimum of the measured signal, corresponding to destructive interference, and moved the stage to that point. We have run several experiments with various time periods between the stabilizations. The highest stability was measured by stabilizing the gate every 100 s. Corresponding median of distances (expressed in fraction of used wavelength) the gate moved from the default point equals to a distance $\frac{\lambda}{170.7}$.

Using similar algorithmic approach, we also minimized the temporal delay between the individual photons of the SPDC pair that served as the input to the quantum gate. In this case, we measured a drop in detection of two-photon coincident counts, which is caused by bunching of the photons as the temporal delay equalizes. The visibility of corresponding Hong-Ou-Mandel dip was measured to the value of $V = 92 \pm 4$ %.

The third chapter described how to machine-learn the built quantum gate to optimally clone qubits for a class of phase-covariant quantum states. The gate formally operates as a polarization dependent beam splitter with tunable splitting ratios for horizontal $|H\rangle$ and vertical $|V\rangle$ polarization states. This tunability provides two parameters for self-learning labeled ϕ and θ throughout the text, while the third learnable parameter ω is embedded in the state of the ancillary photon. The learning is achieved by optimizing the parameters using Nelder–Mead

simplex algorithm. The feedback to the optimization algorithm is represented by measured fidelities F_1 and F_2, which express the quality of both respective clones.

We have conducted two successful cloning experiments and implemented corresponding simulations to validate the measured values. In the first experimental model, the parameter ω was fixed at a value of $\omega = 45°$ and the parameters ϕ, θ converged to the values $\phi = 28.59°$, $\theta = 17.11°$. In the second experiment with three learnable parameters, the algorithm trained the gate to the values $\omega = 41.49°$, $\phi = 27.44°$, $\theta = 21.68°$. The corresponding theoretically optimal values that were acquired by the simulations equal $\omega = 45°$, $\phi = 31.31°$, $\theta = 13.68°$.

In both experiments, the fidelities measured throughout the test set averaged closely to the optimal theoretical limit of $F = 0.854$. We measured values of $F_1 = 0.840 \pm 0.033$, $F_2 = 0.849 \pm 0.040$ for the first experimental model and $F_1 = 0.843 \pm 0.046$, $F_2 = 0.853 \pm 0.022$ for the second experimental model. The fact that the cloner was able to reach the optimal fidelities even though the parameters converged to different values suggests that the cloner was able to counter all experimental imperfections, both in the preparation of the input state and alignment of the device. It was therefore performing better than one would perform strictly adhering to analytical solution, having various experimental imperfections present in the setup.

Bibliography

[1] J. Jašek, K. Jiráková, K. Bartkiewicz, A. Černoch, T. Fürst, and K. Lemr, "Experimental hybrid quantum-classical reinforcement learning by boson sampling: how to train a quantum cloner," *Optics Express*, vol. 27, p. 32454, oct 2019.

[2] D. J. Griffiths, *Introduction to Quantum Mechanics; 2nd ed.* Upper Saddle River, NJ: Pearson, 2005.

[3] V. Giovannetti, S. Lloyd, and L. Maccone, "Advances in quantum metrology," *Nature Photonics*, vol. 5, pp. 222–229, mar 2011.

[4] M. A. Nielsen and I. Chuang, *Quantum computation and quantum information.* Cambridge University Press, 2002.

[5] C. H. Bennett and G. Brassard, "Quantum cryptography: Public key distribution and coin tossing," in *Proceedings IEEE International Conference on Computers, Systems and Signal Processing*, p. 175, IEEE, New York, Dec 1984.

[6] X. Zhang, H.-O. Li, K. Wang, G. Cao, M. Xiao, and G.-P. Guo, "Qubits based on semiconductor quantum dots," *Chinese Physics B*, vol. 27, p. 020305, feb 2018.

[7] N. Friis, O. Marty, C. Maier, C. Hempel, M. Holzäpfel, P. Jurcevic, M. B. Plenio, M. Huber, C. Roos, R. Blatt, and B. Lanyon, "Observation of entangled states of a fully controlled 20-qubit system," *Physical Review X*, vol. 8, apr 2018.

[8] J. Kelly, R. Barends, A. G. Fowler, A. Megrant, E. Jeffrey, T. C. White, D. Sank, J. Y. Mutus, B. Campbell, Y. Chen, Z. Chen, B. Chiaro, A. Dunsworth, I.-C. Hoi, C. Neill, P. J. J. O'Malley, C. Quintana, P. Roushan, A. Vainsencher, J. Wenner, A. N. Cleland, and J. M. Martinis, "State preservation by repetitive error detection in a superconducting quantum circuit," *Nature*, vol. 519, pp. 66–69, mar 2015.

[9] K. Lemr, *Experimental quantum information processing with photon pairs.* PhD thesis, Palacký University Olomouc, 2012.

[10] S. J. Russell and P. Norvig, *Artificial Intelligence: A Modern Approach (2nd Edition).* Prentice Hall, December 2002.

[11] J. Biamonte, P. Wittek, N. Pancotti, P. Rebentrost, N. Wiebe, and S. Lloyd, "Quantum machine learning," *Nature*, vol. 549, pp. 195–202, sep 2017.

[12] P. Rebentrost, M. Mohseni, and S. Lloyd, "Quantum support vector machine for big data classification," *Phys. Rev. Lett.*, vol. 113, p. 130503, Sep 2014.

[13] M. O. Scully and M. S. Zubairy, *Quantum Optics*. Cambridge University Press, 1997.

[14] P. K. Chris Gerry, *Introductory Quantum Optics*. Cambridge University Pr., 2004.

[15] D. J. Griffiths, *Introduction to electrodynamics*. Pearson, 2013.

[16] H. Goldstein, *Classical Mechanics*. Addison-Wesley, 1980.

[17] C. E. Shannon, "A mathematical theory of communication," vol. 27, pp. 379–423,623–656, 1948.

[18] P. C. Humphreys, B. J. Metcalf, J. B. Spring, M. Moore, X.-M. Jin, M. Barbieri, W. S. Kolthammer, and I. A. Walmsley, "Linear optical quantum computing in a single spatial mode," *Physical Review Letters*, vol. 111, oct 2013.

[19] J. Zeuner, A. N. Sharma, M. Tillmann, R. Heilmann, M. Gräfe, A. Moqanaki, A. Szameit, and P. Walther, "Integrated-optics heralded controlled-NOT gate for polarization-encoded qubits," *npj Quantum Information*, vol. 4, feb 2018.

[20] K. H. Kagalwala, G. D. Giuseppe, A. F. Abouraddy, and B. E. A. Saleh, "Single-photon three-qubit quantum logic using spatial light modulators," *Nature Communications*, vol. 8, sep 2017.

[21] M. Kues, C. Reimer, P. Roztocki, L. R. Cortés, S. Sciara, B. Wetzel, Y. Zhang, A. Cino, S. T. Chu, B. E. Little, D. J. Moss, L. Caspani, J. Azaña, and R. Morandotti, "On-chip generation of high-dimensional entangled quantum states and their coherent control," *Nature*, vol. 546, pp. 622–626, jun 2017.

[22] I. Marcikic, H. de Riedmatten, W. Tittel, H. Zbinden, M. Legré, and N. Gisin, "Distribution of time-bin entangled qubits over 50 km of optical fiber," *Physical Review Letters*, vol. 93, oct 2004.

[23] A. Mair, A. Vaziri, G. Weihs, and A. Zeilinger, "Entanglement of the orbital angular momentum states of photons," *Nature*, vol. 412, pp. 313–316, jul 2001.

[24] D. Halliday, R. Resnick, and J. Walkers, *Fundamentals of physics; 6th ed.* New York, NY: Wiley, 2001.

[25] E. Collett, *Field Guide to Polarization*. SPIE, sep 2005.

[26] E. L. O'Neill, *Introduction to Statistical Optics*. Dover Publications Inc., 2004.

[27] R. W. Boyd, *Nonlinear Optics*. Elsevier LTD, Oxford, 2008.

[28] S. Mingaleev and Y. Kivshar, "Nonlinear photonic crystals toward all-optical technologies," *Optics and Photonics News*, vol. 13, p. 48, jul 2002.

[29] G. Weihs and A. Zeilinger, "1 photon statistics at beam splitters : an essential tool in quantum information and teleportation," 2001.

[30] E. Hecht, *Optics, Global Edition*. Pearson, 2016.

[31] B. E. A. Saleh and M. C. Teich, *Fundamentals of photonics; 2nd ed.* Wiley series in pure and applied optics, New York, NY: Wiley, 2007.

[32] W. K. Wootters and W. H. Zurek, "A single quantum cannot be cloned," *Nature*, vol. 299, pp. 802–803, oct 1982.

[33] V. Bužek and M. Hillery, "Quantum copying: Beyond the no-cloning theorem," *Physical Review A*, vol. 54, pp. 1844–1852, sep 1996.

[34] N. J. Cerf and J. Fiurasek, "Optical quantum cloning - a review," 2005.

[35] V. Scarani, S. Iblisdir, N. Gisin, and A. Acín, "Quantum cloning," *Reviews of Modern Physics*, vol. 77, pp. 1225–1256, nov 2005.

[36] D. Bruß, M. Cinchetti, G. M. D'Ariano, and C. Macchiavello, "Phase-covariant quantum cloning," *Physical Review A*, vol. 62, jun 2000.

[37] J. M. Renes, "Spherical-code key-distribution protocols for qubits," *Phys. Rev. A*, vol. 70, p. 052314, Nov 2004.

[38] M. Schiavon, G. Vallone, and P. Villoresi, "Experimental realization of equiangular three-state quantum key distribution," *Scientific Reports*, vol. 6, 03 2016.

[39] N. Gisin and S. Massar, "Optimal quantum cloning machines," *Physical Review Letters*, vol. 79, pp. 2153–2156, sep 1997.

[40] J. Fiurášek, "Optical implementations of the optimal phase-covariant quantum cloning machine," *Physical Review A*, vol. 67, may 2003.

[41] A. Ianevski, A. K. Giri, P. Gautam, A. Kononov, S. Potdar, J. Saarela, K. Wennerberg, and T. Aittokallio, "Prediction of drug combination effects with a minimal set of experiments," *Nature Machine Intelligence*, vol. 1, pp. 568–577, dec 2019.

[42] J. Hecht, "Managing expectations of artificial intelligence," *Nature*, vol. 563, pp. S141–S143, nov 2018.

[43] O. Simeone, "A very brief introduction to machine learning with applications to communication systems," *IEEE Transactions on Cognitive Communications and Networking*, vol. 4, pp. 648–664, dec 2018.

[44] C. M. Bishop, *Pattern Recognition and Machine Learning*. Springer-Verlag New York Inc., 2006.

[45] S. Ruder, "An overview of gradient descent optimization algorithms," 2016.

[46] J. A. Nelder and R. Mead, "A simplex method for function minimization," *The Computer Journal*, vol. 7, pp. 308–313, jan 1965.

[47] D. Silver, A. Huang, C. J. Maddison, A. Guez, L. Sifre, G. van den Driessche, J. Schrittwieser, I. Antonoglou, V. Panneershelvam, M. Lanctot, S. Dieleman, D. Grewe, J. Nham, N. Kalchbrenner, I. Sutskever, T. Lillicrap, M. Leach, K. Kavukcuoglu, T. Graepel, and D. Hassabis, "Mastering the game of go with deep neural networks and tree search," *Nature*, vol. 529, pp. 484–489, jan 2016.

[48] X.-D. Cai, D. Wu, Z.-E. Su, M.-C. Chen, X.-L. Wang, L. Li, N.-L. Liu, C.-Y. Lu, and J.-W. Pan, "Entanglement-based machine learning on a quantum computer," *Phys. Rev. Lett.*, vol. 114, p. 110504, Mar 2015.

[49] M. Schuld and N. Killoran, "Quantum machine learning in feature hilbert spaces," *Phys. Rev. Lett.*, vol. 122, p. 040504, Feb 2019.

[50] A. Hentschel and B. C. Sanders, "Machine learning for precise quantum measurement," *Phys. Rev. Lett.*, vol. 104, p. 063603, Feb 2010.

[51] N. B. Lovett, C. Crosnier, M. Perarnau-Llobet, and B. C. Sanders, "Differential evolution for many-particle adaptive quantum metrology," *Phys. Rev. Lett.*, vol. 110, p. 220501, May 2013.

[52] J. Gao, L.-F. Qiao, Z.-Q. Jiao, Y.-C. Ma, C.-Q. Hu, R.-J. Ren, A.-L. Yang, H. Tang, M.-H. Yung, and X.-M. Jin, "Experimental machine learning of quantum states," *Phys. Rev. Lett.*, vol. 120, p. 240501, Jun 2018.

[53] C. K. Hong, Z. Y. Ou, and L. Mandel, "Measurement of subpicosecond time intervals between two photons by interference," *Physical Review Letters*, vol. 59, pp. 2044–2046, nov 1987.

[54] G. Armendáriz, J. Cravioto-Lagos, V. Velázquez, M. Grether, E. López-Moreno, and E. J. Galvez, "Teaching quantum mechanics with the hong-ou-mandel interferometer," in *12th Education and Training in Optics and Photonics Conference* (M. F. P. C. M. Costa and M. Zghal, eds.), SPIE, jul 2014.

[55] K. Bartkiewicz, A. Černoch, K. Lemr, J. Soubusta, and M. Stobińska, "Efficient amplification of photonic qubits by optimal quantum cloning," *Phys. Rev. A*, vol. 89, p. 062322, Jun 2014.

[56] K. Bartkiewicz, A. Černoch, G. Chimczak, K. Lemr, A. Miranowicz, and F. Nori, "Experimental quantum forgery of quantum optical money," *npj Quantum Information*, vol. 3, p. 7, Mar. 2017.

[57] J. C. Nash, *Compact numerical methods for computers: linear algebra and function minimisation.* CRC press, Bristol (UK), 1990.

[58] J. Soubusta, L. Bartůšková, A. Černoch, J. Fiurášek, and M. Dušek, "Several experimental realizations of symmetric phase-covariant quantum cloners of single-photon qubits," *Phys. Rev. A*, vol. 76, p. 042318, Oct 2007.

[59] J. Soubusta, L. Bartůšková, A. Černoch, M. Dušek, and J. Fiurášek, "Experimental asymmetric phase-covariant quantum cloning of polarization qubits," *Physical Review A*, vol. 78, nov 2008.

[60] J.-S. Xu, C.-F. Li, L. Chen, X.-B. Zou, and G.-C. Guo, "Experimental realization of the optimal universal and phase-covariant quantum cloning machines," *Phys. Rev. A*, vol. 78, p. 032322, Sep 2008.

[61] F. Buscemi, G. M. D'Ariano, and C. Macchiavello, "Economical phase-covariant cloning of qudits," *Phys. Rev. A*, vol. 71, p. 042327, Apr 2005.

Appendix

Confirmation of contribution

As the supervisor and corresponding author of Jan Jašek's publication

- J. Jašek, K. Jiráková, K. Bartkiewicz, A. Černoch, T. Fürst, and K. Lemr, *"Experimental hybrid quantum-classical reinforcement learning by boson sampling: how to train a quantum cloner,"* Opt. Express **27**, 32454 (2019)

I hereby certify that Jan Jašek significantly contributed to the scientific investigation presented in this publication. He implemented the experimental setup, programmed the controlling software and contributed to writing of the manuscript. The extracts of the publication directly quoted in his thesis were predominantly written by him.

Dolní Životice, 19th March 2020

....

doc. Mgr. Karel Lemr, Ph.D.
Joint Laboratory of Optics

Experimental hybrid quantum-classical reinforcement learning by boson sampling: how to train a quantum cloner

Jan Jašek,[1] Kateřina Jiráková,[1] (iD) Karol Bartkiewicz,[1,2] Antonín Černoch,[3] Tomáš Fürst,[4] and Karel Lemr[1,*] (iD)

[1]*RCPTM, Joint Laboratory of Optics of Palacký University and Institute of Physics of Czech Academy of Sciences, 17. listopadu 12, 771 46 Olomouc, Czech Republic*
[2]*Faculty of Physics, Adam Mickiewicz University, PL-61-614 Poznań, Poland*
[3]*Institute of Physics of Czech Academy of Sciences, Joint Laboratory of Optics of PU and IP AS CR, 17. listopadu 50A, 772 07 Olomouc, Czech Republic*
[4]*Department of Mathematical Analysis and Application of Mathematics, Faculty of Science, Palacký University, 17. listopadu 12, 771 46 Olomouc, Czech Republic*
[*]*k.lemr@upol.cz*

Abstract: We report on experimental implementation of a machine-learned quantum gate driven by a classical control. The gate learns optimal phase-covariant cloning in a reinforcement learning scenario having fidelity of the clones as reward. In our experiment, the gate learns to achieve nearly optimal cloning fidelity allowed for this particular class of states. This makes it a proof of present-day feasibility and practical applicability of the hybrid machine learning approach combining quantum information processing with classical control. The quantum information processing performed by the setup is equivalent to boson sampling, which, in complex systems, is predicted to manifest quantum supremacy over classical simulation of linear-optical setups.

1. Introduction

Machine learning methods are extensively used in an increasing number of fields, e.g., automotive industry, medical science, internet security, air-traffic control etc. This field conveys many algorithms and structures ranging from simple linear regression to almost arbitrarily complex neural networks which are able to find solutions to highly complex problems. Recently, a considerable attention was drawn to the overlap between quantum physics and machine learning [1]. Depending on the type of input data and data processing algorithms, we can distinguish four types of quantum machine learning (QML), i.e., CC (classical data and classical data processing – classical limit of quantum machine learning), QC (quantum data and classical data processing), CQ (classical data and quantum data processing), and QQ (quantum data and quantum data processing).

QML offers reduced computational complexity with respect to its classical counterpart in solving some classes of problems [1]. Depending on the problem at hand the speedup can be associated with various features of quantum physics. A number of proposals and experiments focused on QML have been reported, such works include quantum support vector machines [2], Boltzmann machines [3], quantum autoencoders [4], kernel methods [5], and quantum reinforcement learning [6,7]. In reinforcement learning a learning agent receives feedback in order to learn an optimal strategy for handling a nontrivial task. Next, the performance of the agent is tested on cases that were not included in the training. If the agent performs well in these cases, learning is completed. The difference between machine learning and mere optimization is often very subtle. For instance in a recent Letter [3], Gao *et al.* have trained a neural network to classify quantum states according to their capability to violate the CHSH inequality. In that case, a classical computer learned a set of five real-valued numbers used as weight factors in

the sum of correlation coefficients obtained in an already known measurement configuration. In contrast to that, our protocol relies on a feed-back between a classical control and a quantum gate rendering it genuinely quantum-classical machine learning.

Here we demonstrate experimentally that reinforcement learning can be used to train an optical quantum gate (see Fig. 1). This problem is related to the boson sampling [9–13], where one knows the form of the scattering matrix of a system and computes modulus squared of its permanent. However, here we optimize the probabilities of obtaining certain outputs of the gate by finding the optimal parameters of the scattering matrix. Calculating the probabilities (moduli squared of permanents of scattering matrix) is in general a computationally hard task while measuring them is much faster. This feature of quantum optics allows us to expect that complex integrated interferometers could be applied as special-purpose quantum computers (e.g. [14]). This sets our problem in the class of CQ quantum machine learning tasks. There are other QML approaches to optimizing quantum circuits. One approach uses classical machine learning to optimize the design of a quantum experiment in order to produce desired states [15]. Another QML approach consists of optimizing quantum circuits to improve the solution to some problems solved on a quantum computer [16]. The latter method can be applied even to minor computational tasks to save resources [17,18].
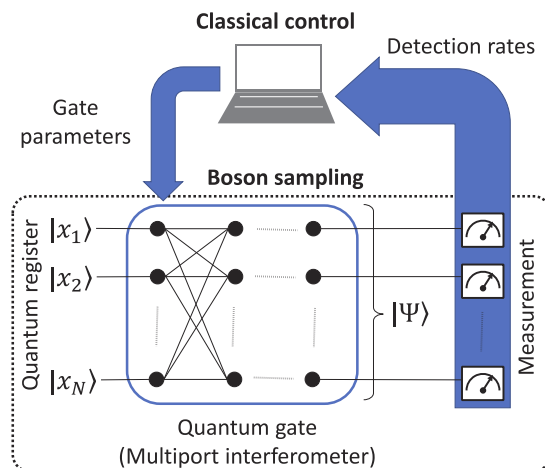

Fig. 1. Conceptual scheme of hybrid reinforcement learning of a quantum gate driven by a classical control. The transformation of the quantum register performed by the gate is evaluated by measurement providing a reward to the classical control that iteratively modifies the gate's parameters. The core of this procedure can be viewed as boson sampling, classical simulation of which is known to be computationally #P-hard in N [8].

We applied online reinforcement learning methods to train an optimal quantum cloner. Quantum cloning is indispensable for safety tests of quantum cryptography systems or of other quantum communications protocols. Perfect quantum cloning of an unknown state is prohibited by the no-cloning theorem [19]. However, it is possible to prepare imperfect clones that resemble the original state to a certain degree. Usually the approach towards quantum cloning involves direct optimization of the experimentally implemented interaction between the system in the cloned state and another systems to maximize the fidelity of the output clones [20]. In contrast to that, we present a quantum gate (learning agent) that is capable to self-learn such interaction (policy) based on provided feedback (implicit setting of the parameters). For the purposes of this

proof-of-principle experiment, we limit ourselves to equatorial qubits in the form of

$$|\psi_s\rangle = 1/\sqrt{2}\left(|0\rangle + e^{i\eta}|1\rangle\right), \tag{1}$$

where $|0\rangle$ and $|1\rangle$ denote logical qubit states. Cloning of these states is known to be the optimal means of individual attack on the famous quantum cryptography protocols BB84 [21] and RO4 [22,23] or quantum money protocol [24] (see also Bartkiewicz *et al.* for experimental implementation [25,26]).

2. Experimental realization

We constructed a device composed of a linear optical quantum gate and a computer performing classical information processing. While the gate itself is capable of a broad range of two qubit transformations, this paper focuses on its ability to act as a phase-covariant quantum cloner. Its figure of merit is the individual fidelity of the output copies. The fidelity of the *j*-th clone $F_j = {}_{in}\langle\psi|\hat{\varrho}_j|\psi\rangle_{in}$ is defined as overlap between the state of the input qubit $|\psi\rangle_{in}$ and the state of the clone $\hat{\varrho}_j$. In case of the state in Eq. (1), the maximum achievable fidelity of symmetric $1 \to 2$ cloning accounts for $F_1 = F_2 = \frac{1}{2}\left(1 + \frac{1}{\sqrt{2}}\right) \approx 0.8535$ [27,28].

The experimental setup is depicted in Fig. 2. Pairs of photons are generated in Type I spontaneous parametric down-conversion occurring in a nonlinear BBO crystal. This crystal is pumped by Coherent Paladin Nd-YAG laser with integrated third harmonic generation of wavelength at $\lambda = 355$ nm. The generated pairs of photons are both horizontally polarized and highly correlated in time.
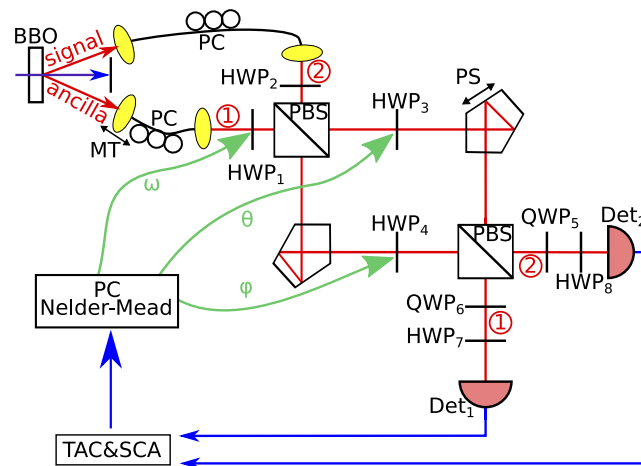

Fig. 2. Experimental setup. Legend: PBS – polarization beam splitter, PC – polarization controller, BBO – beta barium borate, Det – detector, HWP – half-wave plate, QWP – quarter wave-plate, PS – piezoelectric stage, TAC&SCA – time-to-amplitude converter & single channel analyzer.

These photons are then spectrally filtered by 10 nm wide interference filters and spatially filtered by two single mode optical fibers each guiding one photon from the pair. In our experimental setup, qubits are encoded into polarization states of the individual photons ($|0\rangle \Leftrightarrow |H\rangle$ and $|1\rangle \Leftrightarrow |V\rangle$). The photon in the upper path (spatial mode 2) represents the signal qubit, quantum state of which we want to clone, and the photon in the lower path (spatial mode 1) serves as the

ancilla the state of which reads

$$|\psi_a\rangle = \cos 2\omega |H\rangle + \sin 2\omega |V\rangle . \qquad (2)$$

The parameter ω is controlled by the rotation of HWP$_1$ (Fig. 2).

Using polarization controllers (PC) we can ensure that both photons are horizontally polarized at the output of the fibers. Next, polarization states of the photons are set using a combination of half-wave plates (HWPs) and quarter-wave plates (QWPs). There are two stationary QWPs fixed at angle 45° and six motorized HWPs which make it possible to control the whole quantum gate using a computer. The first two half-wave plates HWP$_1$ and HWP$_2$ are used to set polarisation states of the ancilla and cloned photons, respectively.

The core part of the presented quantum gate is a Mach-Zehnder-type interferometer which consists of two polarizing beam splitters (PBS) and two reflective pentaprisms, one of which is attached to the piezoelectric stage (PS). With the addition of two HWPs (HWP$_3$ and HWP$_4$) placed in its arms, this whole interferometer implements a polarization dependent beam splitter with variable splitting ratio. Mathematically, the scattering matrix $\hat{U}$ of the gate transforms the bosonic modes

$$\begin{pmatrix} \hat{a}_{H,1} \\ \hat{a}_{V,1} \\ \hat{a}_{H,2} \\ \hat{a}_{V,2} \end{pmatrix} \rightarrow \begin{pmatrix} \cos 2\phi & 0 & \sin 2\phi & 0 \\ 0 & \cos 2\theta & 0 & \sin 2\theta \\ -\sin 2\phi & 0 & \cos 2\phi & 0 \\ 0 & -\sin 2\theta & 0 & \cos 2\theta \end{pmatrix} \begin{pmatrix} \hat{a}_{H,1} \\ \hat{a}_{V,1} \\ \hat{a}_{H,2} \\ \hat{a}_{V,2} \end{pmatrix}, \qquad (3)$$

where $\hat{a}_{x,i}$ represents the annihilation operators of the individual input, polarization ($x \in \{H,V\}$) as well as spatial ($i \in \{1,2\}$), modes. The angles θ and ϕ correspond to the rotations of HWP$_3$ and HWP$_4$ with respect to the horizontal axis. The transformation (3) is formally equivalent to the transformation by a polarization dependent beam splitter, the intensity splitting ratios of which for horizontal and vertical polarizations are $\cot^2 2\phi$ and $\cot^2 2\theta$, respectively.

The two spatial modes at the output of the interferometer are subjected to polarization projection (QWP$_5$, QWP$_6$ and HWP$_7$, HWP$_8$) and then led to a pair of avalanche photodiodes by Perkin-Elmer running in Geiger mode. We use detection electronics to register both single photons at each of the detectors and coincident detections as successful operation of the gate is indicated by the presence of single photon in each output of the interferometer. The electronic signal is then sent to a classical computer.

For specific parameters of the presented linear-optical elements, this quantum gate functions as a $1 \rightarrow 2$ symmetric phase-covariant cloner, optimal analytical cloning transformation of which is well known [27]. On a linear-optical platform, this optimal cloning transformation can be achieved by a polarization dependent beam splitter with intensity transmissivities for horizontal and vertical polarization at $t_H \approx 0.21$ and $t_V \approx 0.79$, while setting the ancilla to be horizontally polarized. Note that our quantum gate is capable of implementing this transformation when set approximately to $\phi = 31.3, \theta = 13.7$. To showcase the capability of our gate to learn to clone phase-covariant states optimally, we deliberately ignore this analytical solution and employ self-optimization procedure seeking to maximize the cloning fidelities. The optimization process consists of a number of measurements (runs), each performed for a set of variable optimization parameters ϕ, θ, ω. That is, variable splitting ratio for horizontal (ϕ) and vertical (θ) polarization as well as the state of the ancilla (ω) [Eq. (2)]. In each run, output clones fidelities are evaluated and supplied to the classical Nelder-Mead algorithm [29] for a decision about the parameters of the future runs.

In between any two runs, the setup is stabilized. We first minimize temporal delay between the two individual photons. In this case, all HWPs are set to 0° with the exception of HWP$_4$

being at 22.5°. In this regime, we minimize the number of two-photon coincident detections (Hong-Ou-Mandel dip) by changing the temporal delay between the photons using a motorized translation stage MT. In the next step, the phase is stabilized in the interferometer. Moreover, we make use of the fact that the phase shift in the interferometer additively contributes to the phase η of the signal state [Eq. (1)]. This allows us to use interferometer phase stabilization for setting of any signal state of the equatorial class. We achieve this task by setting HWP_2 to 22.5° and HWP_8 to the value corresponding to orthogonal state with respect to the required input signal state. All other HWPs are set to 0° and a minimum in single-photon detections on Det 2 is found by tuning the voltage applied to PS. Note that the entire stabilization procedure is completely independent of the learning process itself.

In this reinforced-learning scenario, the cloner is trained on a sequence of random equatorial signal states [Eq. (1)] different for each run. The phase η is randomly picked from interval $(0; 2\pi)$. The fidelities are obtained by measuring coincidence detections in four different projection settings. We label these coincident detections cc_{ij}, where $i, j \in \{\|; \perp\}$. The $\|$ and the $\perp$ sign denote projection on the signal state $|\psi_s\rangle$ and its orthogonal counterpart $|\psi_s^\perp\rangle$. We calculate the fidelities as $F_1 = \left(cc_{\|\|} + cc_{\|\perp}\right)/\Sigma$ and $F_2 = \left(cc_{\|\|} + cc_{\perp\|}\right)/\Sigma$, where Σ denotes $cc_{\|\|} + cc_{\|\perp} + cc_{\perp\|} + cc_{\perp\perp}$.

To see the connection between boson sampling (i.e., sampling probabilities corresponding to a permanent of scattering matrix) and the optimal quantum cloning let us consider scattering matrix $\hat{U}$ [see Eq. (3)] defined in Fock space of both spatial and polarization modes. This matrix, when optimized, describes the desired optimal quantum operation. Let us also consider a unitary scattering matrix $\hat{S}$, which transforms a single H–polarized photon into the sampled state $|\psi_s\rangle = \hat{S}^\dagger |1_{H,1}, 0_{V,1}\rangle = \alpha |1_{H,1}, 0_{V,1}\rangle + \beta |0_{H,1}, 1_{V,1}\rangle$, where $|\alpha|^2 + |\beta|^2 = 1$. Global cloning fidelity F_G for $1 \rightarrow 2$ phase-covariant cloning can be expressed in terms of the measured detection rates as

$$F_G = \frac{cc_{\|\|}}{\Sigma} = |\langle 1_{H,1}, 0_{V,1}, 1_{H,2}, 0_{V,1}| \hat{S}^{\otimes 2} \hat{U}^\dagger \hat{S} \otimes \hat{1} |1_{H,1}, 0_{V,1}, 1_{H,2}, 0_{V,1}\rangle|^2 = \text{perm}^2[\hat{G}_{\text{odd}}], \quad (4)$$

where $\text{perm}[\hat{G}_{\text{odd}}]$ is the permanent of a matrix [9] constructed by removing even rows and columns from the composite scattering matrix $\hat{G} = \hat{S}^{\otimes 2} \hat{U}^\dagger \hat{S} \otimes \hat{1}$ and $\hat{1}$ is the identity operator acting on the relevant part of the Fock space. Similarly, for an ancilla-free process delivering N clones from M copies of qubits we can define global fidelity as $F_G = \text{perm}^2[\hat{G}_{\text{odd}}]$ for $\hat{G}_{\text{odd}}$ constructed from $\hat{G} = \hat{S}^{\otimes N} \hat{U}^\dagger \hat{S}^{\otimes M} \otimes \hat{1}$. Similarly as before, the global fidelity is associated with permanent of the scattering matrix [9] which governs the evolution of bosons undergoing arbitrary unitary transformation. Simulating outcomes of such scattering process on a classical computer is known to be #P–hard [8] and becomes exponentially harder with the number of photons and polynomially harder with the number of output modes [30]. Considering that the number of iterations needed for the Nelder-Mead algorithm to converge grows linearly with the number of parameters of a quadratic cost function [31,32], the predominantly demanding computational task is the calculations of permanents (simulation of boson sampling). When we analyze the clones independently, the relevant figure of merit is the already introduced local fidelity that in our experiment reads

$$F_1 = F_G + \frac{cc_{\|\perp}}{\Sigma}, \qquad F_2 = F_G + \frac{cc_{\perp\|}}{\Sigma}. \quad (5)$$

However, for larger system applying global fidelity as a figure of merit is more practical [20]. Note that similarly as in case of global fidelity we can express the remaining detection rates $\frac{cc_{ij}}{\Sigma}$ for $i \neq j$ as permanents, i.e.,

$$\frac{cc_{\|\perp}}{\Sigma} = |\langle 1_{H,1}, 0_{V,1}, 0_{H,2}, 1_{V,1}| \hat{S}^{\otimes 2} \hat{U}^\dagger \hat{S} \otimes \hat{1} |1_{H,1}, 0_{V,1}, 1_{H,2}, 0_{V,1}\rangle|^2 = \text{perm}^2[\hat{G}_{\|\perp}], \quad (6)$$

and

$$\frac{cc_{\perp\|}}{\Sigma} = |\langle 0_{H,1}, 1_{V,1}, 1_{H,2}, 0_{V,1}| \hat{S}^{\otimes 2} \hat{U}^\dagger \hat{S} \otimes \hat{1} |1_{H,1}, 0_{V,1}, 1_{H,2}, 0_{V,1}\rangle|^2 = \text{perm}^2[\hat{G}_{\|\perp}], \quad (7)$$

where $\hat{G}_{\|\perp}$ ($\hat{G}_{\perp\|}$) are constructed by removing even rows and columns 2, 3 (1, 4) from the composite scattering matrix $\hat{G}$. Thus, for evaluating single-copy fidelities of $1 \rightarrow 2$ cloning we need to evaluate 2 permanents more than for evaluating global fidelity.

Note that in the experiment, we do not measure the permanent itself but rather its modulus squared. Further to that, we only consider cases when 0 or 1 photon is present in an output mode. Thus, we avoid the problem of exponentially small detection probabilities of higher photon-number states [see Eq. (4)]. As a result, our measurement scales better that classical methods of calculating permanents.

3. Results

We demonstrate reinforcement-learned quantum cloner for a class of phase-covariant quantum states. The gate operates formally as a polarization dependent beam splitter with tunable splitting ratios. This tunability provides two parameters for self-learning, ϕ and θ. The third learnable parameter ω is embedded in the state of the ancillary photon [Eq. (2)]. We have experimentally implemented two machine learning models using two and three parameters, respectively. In the first model, we fixed the ancilla state to its theoretically known optimum $|\psi_{\mathrm{a}}\rangle = |H\rangle$. The remaining two parameters, ϕ and θ, were machine learned. To minimize the cost function (i.e. optimize the performance of the cloner) we applied Nelder-Mead simplex algorithm which iteratively searches for a minimum of a cost function. We chose the cost function to be in the form of $C = (1 - F_1)^2 + (1 - F_2)^2 + (F_1 - F_2)^2$, where F_1 and F_2 stand for the fidelity of the first and second clone, respectively. This choice reflects the natural requirements to obtain maximum fidelities of both the clones as well as to force the cloner into a symmetrical cloning regime. Training of the gate consists of providing it with training instances of equatorial qubit states (randomly generated in each cost function evaluation, i. e. an online machine learning scenario) and with the respective fidelity of the clones. In each training run, the underlying Nelder-Mead algorithm sets the gate parameters to vertices of simplexes in the parameter space and then decides on a future action. In the case of a two-parameter optimization, these simplexes correspond to triangles as depicted in Fig. 3. In this figure, we plot the exact path taken by the Nelder-Mead simplex algorithm to minimize the cost function C for the case of a real experiment and its simulation. The selected initial simplex was intentionally chosen well away from the optimal position – its first vertex resembles the trivial cloning strategy [26,33]. In Fig. 4(a), we illustrate the evolution of both the fidelities F_1 and F_2 during the training. After 40 runs (i.e. 40 instances from the training set), this model was deemed trained because the size of simplexes dropped to the experimental uncertainty level (i.e. ~ 0.1 degrees on rotation angles of wave plates). However, in general, setting the simplex to converge within a given precision is a nontrivial problem [34].

In the second model, we let the gate learn the optimal setting of the ancilla ω along with the gate parameters ϕ and θ. The training procedure ran similarly to the first model. The initial value of the ω parameter was set naively to $\omega = \frac{\pi}{8}$ so it lied on the equator of the Poincaré-Bloch sphere. We present evolution of the intermediate fidelities of this three-parameter model in Fig. 4(b). Using a similar stopping criterion as in the first model, the training of the second model was terminated after 60 runs.

We have tested the performance of both our models on independent random test sets each populated by 40 instances of equatorial states. We summarize the results of the two models in Table 1, where we provide the final learned parameters together with the mean values of the fidelities on the test sets $\langle F_1 \rangle$ and $\langle F_2 \rangle$. The observed fidelities on test sets are bordering on the theoretical limit (at most 0.013 below it) which renders our gate highly precise in context of previously implemented cloners [27,35–39].
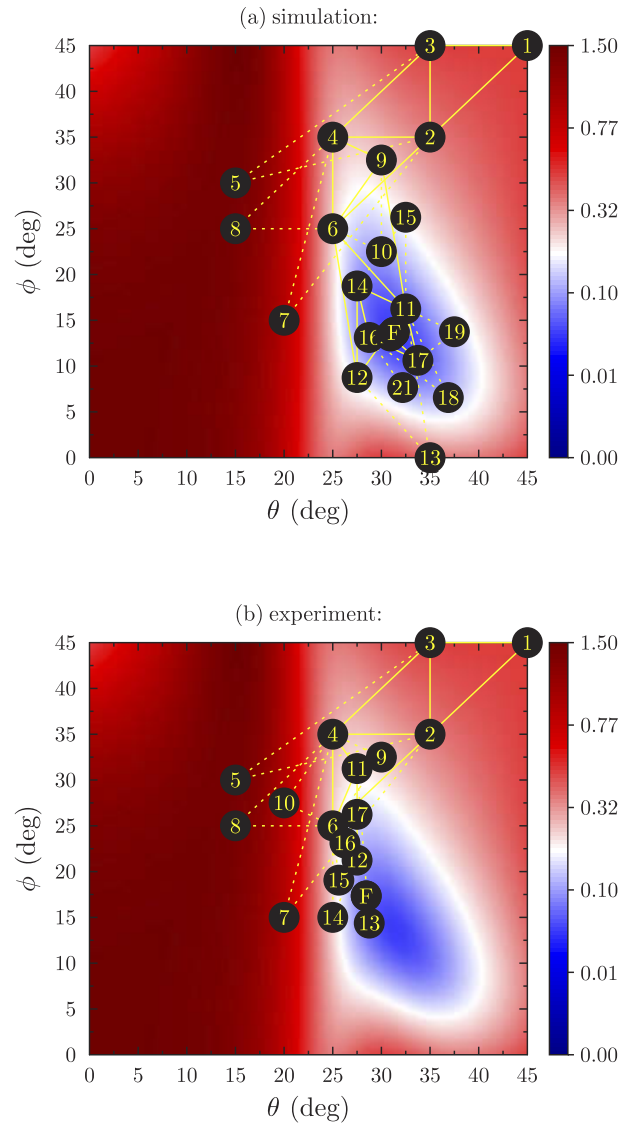
Fig. 3. Plot of the cost function C for the angles ϕ and θ (corresponding to HWP_4 and HWP_3 in Fig. 2, respectively). The solid yellow lines denote the final triangles reached by the Nelder–Mead simplex minimization [29] algorithm in each of its iteration. The dashed lines mark intermediate steps. The circled numbers stand for gate runs and point F depicts the final state of the gate at the end of training. A simulation was performed prior to the experiment to verify our implementation of the learning algorithm. Note that the starting simplex is chosen in advance and is identical in both cases. Subsequent paths in case of the simulation and actual experiment differ due to setup imperfections.
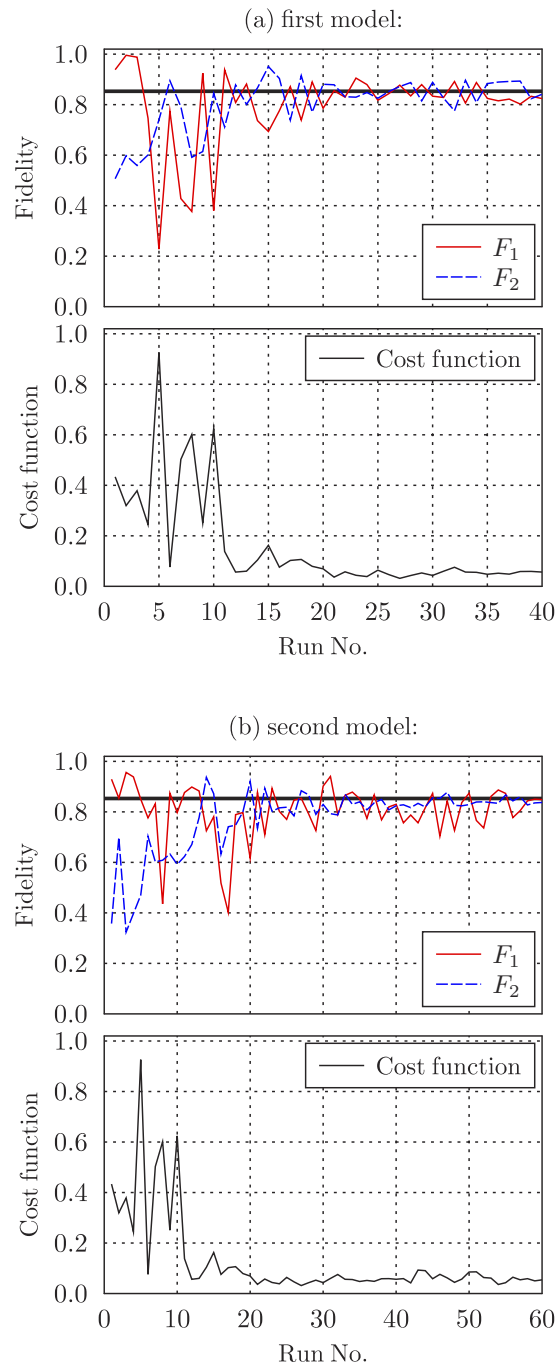
(a) first model:

(b) second model:

Fig. 4. Plots showing the evolution of fidelity of both the clones (top) as well as the cost function (bottom) throughout the training in case of (a) the first model with two free parameters ϕ and θ and (b) the second model with three free parameters ϕ, θ and ω. Fidelity of the first clone F_1 is visualized by a solid red line and the fidelity of the second clone F_2 is shown in blue (dashed line). The thick solid black line stands for the theoretical limit of ≈ 0.8535. This theoretical limit bounds the value of fidelity averaged over both clones and over all equatorial states. It is legitimate and expected for F_1 to be close to 1 as the cloner starts in a highly asymmetric regime. Moreover, slight deviation from perfect sampling of equatorial input states can cause the average fidelity to surpass the theoretical limit by a few percent.

Table 1. Summary of the Final Values for Both Models. $\langle F_1 \rangle$ and $\langle F_2 \rangle$ Denote the Mean Fidelities Observed on the Test Sets.

Final values	Model 1	Model 2
training:		
Angle ϕ	28.59	27.44
Angle θ	17.11	21.68
Angle ω	45°(fixed)	41.49°
No. of training	40	60
instances (runs)		
testing:		
$\langle F_1 \rangle$	0.840 ± 0.033	0.849 ± 0.040
$\langle F_2 \rangle$	0.843 ± 0.046	0.853 ± 0.022

4. Conclusions

In our proof of principle experiment, we implemented a CQ reinforcement quantum machine learning algorithm driven by a hybrid of classical Nelder–Mead method and quantum computing performed as a measurement of modulus squared of a permanent. This approach was used to train a practical quantum gate (i.e., a quantum cloner). The task of the training was to optimize parameters of the gate (interferometer) ϕ, θ and ω (setting of the ancilla in the second experiment) to perform phase-covariant cloning. The quality of both the clones measured by their fidelities F_1 and F_2 which were evaluated within both experiments (Fig. 4) successfully reached the theoretical limit for phase-covariant cloning 0.854. Remarkably, the cloner managed to achieve almost optimal cloning by learning setup parameters, slightly different from analytical values, that counter all experimental imperfections including imperfections in the cloner itself and in the input state preparation.

To see the connection between boson sampling and our results, let us focus on computing the modulus squared of the permanent perm[$\hat{U}$] of scattering matrix describing the gate operation. The unitary scattering matrix $\hat{U}$ performs linear transformation on the annihilation operators $\hat{a}_i$ of the input modes (i can be an index labeling both the polarization and the spatial degrees of freedom). Then the input-output relation of an quantum-optical interferometer is given as $\hat{b}_j = \sum \hat{U}_{i,j}^{\dagger} \hat{a}_i$. If all the input modes of an interferometer are injected with single photons and single photons are detected at specific outputs (no bunching) the probability of obtaining the desired detection coincidence is $p = |\text{perm}[\hat{U}]|^2$. However, this expression becomes more complex if some modes are occupied by more than one photon. Then factorials of mode-specific photon numbers appear as denominator and the respective rows/columns of U must be repeated a corresponding number of times [9]. If some output modes are not to be populated, the respective row of $\hat{U}$ matrix is deleted. Calculating the moduli squared of permanents of the scattering matrix associated with our cloner by hand is already challenging (we have polarization and spatial degrees of freedom for two photons) and in general it falls into the #*P*-hard complexity class. The quantum information processing performed by the setup is equivalent to boson sampling which, in complex systems, is predicted to manifest quantum supremacy over classical simulation of linear-optical setups. This makes our research a relevant application of so-called quantum circuit learning described in [40], Mitarai *et al.* The integrated-optics platform [13] or superconducting qubits [41] seem to be promising platforms for large-scale quantum machine learning of this type.

Our results also opens possibilities of further research or applications in the field of quantum key distribution. Suppose a typical attack on the key distribution scheme: Bob and Alice share quantum states and the attacker Eve is eavesdropping on them. Bob and Alice exchange quantum states and, via a classical line, they can decide to stop exchanging qubits (because of noise). Let

us assume that Eve is eavesdropping on both quantum and classical communication. Eve can in principle use reinforcement learning to train a cloner to perform the attack by feeding it with information on the behavior of Bob and Alice, e.g., their decision on continuing or aborting the exchange of a quantum key and/or their decision on parameters of privacy amplification. For such application the proposed gate would have to be modified since Eve does not know the specific class of states used by Bob and Alice, but that is out of the scope of this paper.

Funding

Disclosures

The authors declare no conflicts of interest.

References

1. J. Biamonte, P. Wittek, N. Pancotti, P. Rebentrost, N. Wiebe, and S. Lloyd, "Quantum machine learning," Nature **549**(7671), 195–202 (2017).
2. X.-D. Cai, D. Wu, Z.-E. Su, M.-C. Chen, X.-L. Wang, L. Li, N.-L. Liu, C.-Y. Lu, and J.-W. Pan, "Entanglement-based machine learning on a quantum computer," Phys. Rev. Lett. **114**(11), 110504 (2015).
3. J. Gao, L.-F. Qiao, Z.-Q. Jiao, Y.-C. Ma, C.-Q. Hu, R.-J. Ren, A.-L. Yang, H. Tang, M.-H. Yung, and X.-M. Jin, "Experimental machine learning of quantum states," Phys. Rev. Lett. **120**(24), 240501 (2018).
4. A. Pepper, N. Tischler, and G. J. Pryde, "Experimental realization of a quantum autoencoder: The compression of qutrits via machine learning," Phys. Rev. Lett. **122**(6), 060501 (2019).
5. M. Schuld and N. Killoran, "Quantum machine learning in feature hilbert spaces," Phys. Rev. Lett. **122**(4), 040504 (2019).
6. A. Hentschel and B. C. Sanders, "Machine learning for precise quantum measurement," Phys. Rev. Lett. **104**(6), 063603 (2010).
7. N. B. Lovett, C. Crosnier, M. Perarnau-Llobet, and B. C. Sanders, "Differential evolution for many-particle adaptive quantum metrology," Phys. Rev. Lett. **110**(22), 220501 (2013).
8. L. Valiant, "The complexity of computing the permanent," Theor. Comput. Sci. **8**(2), 189–201 (1979).
9. S. Aaronson and A. Arkhipov, "The computational complexity of linear optics," Theory Comput. **9**(1), 143–252 (2013).
10. M. A. Broome, A. Fedrizzi, S. Rahimi-Keshari, J. Dove, S. Aaronson, T. C. Ralph, and A. G. White, "Photonic boson sampling in a tunable circuit," Science **339**(6121), 794–798 (2013).
11. J. B. Spring, B. J. Metcalf, P. C. Humphreys, W. S. Kolthammer, X.-M. Jin, M. Barbieri, A. Datta, N. Thomas-Peter, N. K. Langford, D. Kundys, J. C. Gates, B. J. Smith, P. G. R. Smith, and I. A. Walmsley, "Boson sampling on a photonic chip," Science **339**(6121), 798–801 (2013).
12. M. Tillmann, B. Dakić, R. Heilmann, S. Nolte, A. Szameit, and P. Walther, "Experimental boson sampling," Nat. Photonics **7**(7), 540–544 (2013).
13. A. Crespi, R. Osellame, R. Ramponi, D. J. Brod, E. F. Galvão, N. Spagnolo, C. Vitelli, E. Maiorino, P. Mataloni, and F. Sciarrino, "Integrated multimode interferometers with arbitrary designs for photonic boson sampling," Nat. Photonics **7**(7), 545–549 (2013).
14. Y. Shen, N. C. Harris, S. Skirlo, M. Prabhu, T. Baehr-Jones, M. Hochberg, X. Sun, S. Zhao, H. Larochelle, D. Englund, and M. Soljacic, "Deep learning with coherent nanophotonic circuits," Nat. Photonics **11**(7), 441–446 (2017).
15. L. O'Driscoll, R. Nichols, and P. A. Knott, "A hybrid machine-learning algorithm for designing quantum experiments," https://arxiv.org/abs/1812.03183.
16. G. Giacomo Guerreschi and M. Smelyanskiy, "Practical optimization for hybrid quantum-classical algorithms," https://arxiv.org/abs/1701.01450.
17. J. R. McClean, J. Romero, R. Babbush, and A. Aspuru-Guzik, "The theory of variational hybrid quantum-classical algorithms," New J. Phys. **18**(2), 023023 (2016).
18. A. Peruzzo, J. McClean, P. Shadbolt, M.-H. Yung, X.-Q. Zhou, P. J. Love, A. Aspuru-Guzik, and J. L. O'Brien, "A variational eigenvalue solver on a photonic quantum processor," Nat. Commun. **5**(1), 4213 (2014).
19. W. K. Wootters and W. H. Zurek, "A single quantum cannot be cloned," Nature **299**(5886), 802–803 (1982).
20. H. Fan, Y.-N. Wang, L. Jing, J.-D. Yue, H.-D. Shi, Y.-L. Zhang, and L.-Z. Mu, "Quantum cloning machines and the applications," Phys. Rep. **544**(3), 241–322 (2014).

21. C. H. Bennett and G. Brassard, "Quantum cryptography: Public key distribution and coin tossing," in *Proceedings IEEE International Conference on Computers, Systems and Signal Processing*, vol. 1 (IEEE, 1984), pp. 175–179.
22. J. M. Renes, "Spherical-code key-distribution protocols for qubits," Phys. Rev. A **70**(5), 052314 (2004).
23. M. Schiavon, G. Vallone, and P. Villoresi, "Experimental realization of equiangular three-state quantum key distribution," Sci. Rep. **6**(1), 30089 (2016).
24. S. Wiesner, "Conjugate coding, Original manuscript written circa 1970," SIGACT News **15**(1), 78–88 (1983).
25. K. Bartkiewicz, K. Lemr, A. Černoch, J. Soubusta, and A. Miranowicz, "Experimental eavesdropping based on optimal quantum cloning," Phys. Rev. Lett. **110**(17), 173601 (2013).
26. K. Bartkiewicz, A. Černoch, G. Chimczak, K. Lemr, A. Miranowicz, and F. Nori, "Experimental quantum forgery of quantum optical money," npj Quantum Inf. **3**(1), 7 (2017).
27. J. Fiurášek, "Optical implementations of the optimal phase-covariant quantum cloning machine," Phys. Rev. A **67**(5), 052314 (2003).
28. K. Bartkiewicz, A. Miranowicz, and Ş. K. Özdemir, "Optimal mirror phase-covariant cloning," Phys. Rev. A **80**(3), 032306 (2009).
29. J. A. Nelder and R. Mead, "A simplex method for function minimization," Comput. J. **7**(4), 308–313 (1965).
30. P. Clifford and R. Clifford, "The classical complexity of boson sampling," in *Proceedings of the Twenty-Ninth Annual ACM-SIAM Symposium on Discrete Algorithms*, (Society for Industrial and Applied Mathematics, 2018), pp. 146–155.
31. L. Han and M. Neumann, "Effect of dimensionality on the nelder-mead simplex method," Optim. Methods Softw. **21**(1), 1–16 (2006).
32. M. Baudin, *Nelder-Mead User's Manual* (Scilab Consortium, 2010).
33. K. Bartkiewicz, A. Černoch, K. Lemr, J. Soubusta, and M. Stobińska, "Efficient amplification of photonic qubits by optimal quantum cloning," Phys. Rev. A **89**(6), 062322 (2014).
34. J. C. Nash, *Compact Numerical Methods for Computers: Linear Algebra and Function Minimisation* (CRC Press, 1990).
35. J. Soubusta, L. Bartůšková, A. Černoch, J. Fiurášek, and M. Dušek, "Several experimental realizations of symmetric phase-covariant quantum cloners of single-photon qubits," Phys. Rev. A **76**(4), 042318 (2007).
36. J. Soubusta, L. Bartůšková, A. Černoch, M. Dušek, and J. Fiurášek, "Experimental asymmetric phase-covariant quantum cloning of polarization qubits," Phys. Rev. A **78**(5), 052323 (2008).
37. D. Bruß, M. Cinchetti, M. G. D'Ariano, and C. Macchiavello, "Phase-covariant quantum cloning," Phys. Rev. A **62**(1), 012302 (2000).
38. J.-S. Xu, C.-F. Li, L. Chen, X.-B. Zou, and G.-C. Guo, "Experimental realization of the optimal universal and phase-covariant quantum cloning machines," Phys. Rev. A **78**(3), 032322 (2008).
39. F. Buscemi, G. M. D'Ariano, and C. Macchiavello, "Economical phase-covariant cloning of qudits," Phys. Rev. A **71**(4), 042327 (2005).
40. K. Mitarai, M. Negoro, M. Kitagawa, and K. Fujii, "Quantum circuit learning," Phys. Rev. A **98**(3), 032309 (2018).
41. IBM Quantum, "IBM Quantum Experience," www.research.ibm.com/ibm-q/.